

**An uncertainty-focused approach to modeling the
atmospheric chemistry of persistent organic
pollutants**

by

Colin Michael Pike-Thackray

Submitted to the Department of Earth, Atmospheric, and Planetary
Science

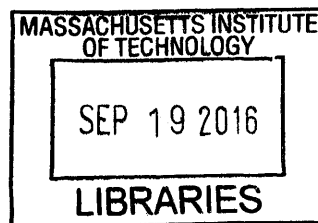
in partial fulfillment of the requirements for the degree of

Doctor of Philosophy

at the

MASSACHUSETTS INSTITUTE OF TECHNOLOGY

September 2016



ARCHIVES

© Massachusetts Institute of Technology 2016. All rights reserved.

Signature redacted

Author

Department of Earth, Atmospheric, and Planetary Science

August 31, 2016

Signature redacted

Certified by

Noelle Eckley Selin

Esther and Harold E. Edgerton Career Development Associate Professor

Thesis Supervisor

Signature redacted

Accepted by

Robert D. van der Hilst

Schlumberger Professor of Earth and Planetary Sciences, Department of

Earth, Atmospheric, and Planetary Sciences

An uncertainty-focused approach to modeling the atmospheric chemistry of persistent organic pollutants

by

Colin Michael Pike-Thackray

Submitted to the Department of Earth, Atmospheric, and Planetary Science
on August 31, 2016, in partial fulfillment of the
requirements for the degree of
Doctor of Philosophy

Abstract

In this thesis, I study polycyclic aromatic hydrocarbons (PAHs) and perfluorocarboxylic acids (PFCAs). PAHs are by-products of burning and therefore have important anthropogenic sources in the combustion of fuels, biomass, etc. PFCAs and their atmospheric precursors are used in making firefighting foams, non-stick coatings, and other surfactant applications.

I quantitatively examine the relative importance of uncertainty in emissions and physicochemical properties (including reaction rate constants) to Northern Hemisphere (NH) and Arctic PAH concentrations. NH average concentrations are more sensitive to uncertainty in the atmospheric lifetime than to emissions rate. The largest uncertainty reductions would come from precise experimental determination of PHE, PYR and BaP rate constants for the reaction with OH.

I calculate long-chain PFCA formation theoretical maximum yields for the degradation of precursor species at a representative sample of atmospheric conditions from a three dimensional chemical transport model, finding that atmospheric conditions farther from pollution sources have both higher capacities to form long chain PFCAs and higher uncertainties in those capacities.

I present results from newly developed simulations of atmospheric PFCA formation and fate using the chemical transport model GEOS-Chem, simulating the degradation of fluorotelomer precursors, as well as deposition and transport of the precursors, intermediates and end-products of the PFCA formation chemistry. I compare the model results to remote deposition measurements and find that it reproduces Arctic deposition of PFOA effectively. Given the most recent precursor emission inventory, the atmospheric indirect source of PFOA and PFNA is 10-45 t/yr globally and 0.2-0.7 t/yr to the Arctic.

Thesis Supervisor: Noelle Eckley Selin

Title: Esther and Harold E. Edgerton Career Development Associate Professor

Acknowledgments

First and foremost, thanks to my advisor Noelle Selin for the opportunity to do this enjoyable and interesting work. Noelle has been the perfect advisor over my time at MIT, allowing me to pursue my own lines of scientific inquiry, while also keeping me on track and seeing the big picture. Special thanks also goes to Jesse Kroll and Ron Prinn, who were both excellent teachers and provided support as thesis committee members, and to Cora Young for her input as an external committee member. Carey Friedman also deserves a special thanks for introducing me in a practical way to the POPs world and to GEOS-Chem.

This work was supported by the U.S. National Science Foundation Arctic Natural Sciences Program (#1203526) and the Atmospheric Chemistry Program (#1053658) and a fellowship from the National Science and Engineering Research Council of Canada. Thanks Marta Venier and Ronald Hites (Indiana University) and Hayley Hung and the Northern Contaminants Program (Environment Canada) for PAH observational data. Thanks to my co-authors in the various works included in this thesis: Carey Friedman, Yanxu Zhang, and Noelle Selin.

Thanks to the entire Selin Group for their diverse input at all stages of my work from proposal to defense, for the friendly work environment, and for exposing me to such a broad range of environmental science and policy ideas. Thanks to the EAPS department's faculty, students and staff for turning my time spent in the Green building into an all-around great experience. Thanks Andy, Vince, Daniel, Sarvesh, Daniel, Michael, Daniel, Sophie, Emily, et al. for occasionally having something other than science to talk about. Finally, for obvious reasons, thanks to my parents and most importantly, Kelly.

Contents

1	Introduction	17
1.1	Motivation for studying PAHs and PFCAs in the atmosphere	17
1.2	Main tools	21
1.2.1	GEOS-Chem atmospheric chemical transport model	21
1.2.2	Polynomial chaos expansions for uncertainty analysis	22
1.3	Overview	24
2	Quantitative assessment of parametric uncertainty in Northern Hemisphere PAH concentrations	25
2.1	Abstract	25
2.2	Introduction	26
2.3	Methods	28
2.3.1	GEOS-Chem Model	29
2.3.2	Polynomial chaos	30
2.3.3	Physicochemical parameter uncertainties	31
2.3.4	Regional emissions uncertainties	33
2.3.5	In-situ observations	34
2.3.6	Constraint of physicochemical parameters by observations	35
2.4	Results	36
2.4.1	Comparison to measurements	36
2.4.2	Contributors to model parametric uncertainty	37
2.4.3	Observation-constrained parameter distributions	39
2.5	Discussion	40

2.6	Selected Supporting Information	44
2.6.1	Tables 2.2 - 2.4 data sources	53
3	Uncertainty and variability in atmospheric PFCA formation	55
3.1	Abstract	55
3.2	Introduction	56
3.3	Methods	58
3.3.1	Mechanism and Box Model	58
3.3.2	Variability of PFCA formation	59
3.3.3	Uncertainty Propagation	61
3.3.4	Environment Categorization	62
3.4	Results	63
3.4.1	Variability in yields due to photochemical environment	63
3.4.2	Uncertainty in yields due to rate constant uncertainty	64
3.4.3	Rate coefficient contributions to yield uncertainty	64
3.4.4	Regime behavior in PFNA yields and formation times	65
3.5	Discussion	66
3.6	Conclusions	71
4	GEOS-Chem simulations of atmospheric PFCA formation	77
4.1	Abstract	77
4.2	Introduction	78
4.3	Materials and Methods	79
4.3.1	PFCA formation chemistry model	80
4.3.2	Comparison to observations	81
4.4	Results	82
4.4.1	Measurement comparison at remote sites	82
4.4.2	Deposition of PFCAs	83
4.4.3	Yields of PFCAs	84
4.5	Discussion	85

List of Figures

2-1	Measured and simulated total (gas and particulate) concentrations at non-urban sites for PHE (top), PYR (middle), and BaP (bottom). The black lines are means across the measurements at all non-urban sites, and their error bars show the standard deviation of the mean for each month. The blue lines are the simulated means across the same sites, with the shaded regions marking the σ and 2σ intervals of the parametric uncertainty distributions for each month.	45
2-2	Constraint of parameter uncertainty distributions by measurement data. (a) PHE, (b) PYR, (c) BaP distributions for the two most important parameters each. Prior distributions (dashed lines), observation-based likelihoods (dot-dashed lines), and posterior distributions (solid lines) shown	46
2-3	Total surface atmospheric concentration uncertainty distributions for BaP (blue), PYR (red), and PHE (green). Annual average (solid lines), winter average (dot-dashed lines), and summer average (dotted lines) shown for both Northern Hemispheric (top) and Arctic (bottom) spatial averages.	47
3-1	Each line represents a different reaction and each node represents a different intermediate species or end product. Reactions are color coded by the non-fluorinated reactant involved.	60

3-2	Histograms of variability in PFOA (a and b) and PFNA (c and d) theoretical maximum yields for both summer (a and c) and winter (b and d) conditions. Each count corresponds to a GEOS-Chem grid-box's output photochemical environment.	74
3-3	Uncertainty distributions of PFOA (left) and PFNA (right) yields for urban, ocean, and Arctic conditions. In both cases, urban yields are much less than 1%	74
3-4	(a) Each photochemical environment plotted in yield-formation time space. Color indicates membership of a cluster in OH-HO ₂ -NO space. Black circles indicate unclustered points. (b) Geographic location of clusters. Colors correspond to the same clusters in both figures. . . .	75
3-5	Total flux through each reaction for the degradation mechanism for urban (a), ocean (b) and Arctic (c) conditions. Each line represents a reaction, with color of the line indicating the photochemical family of the non-fluorinated reactant, and the thickness of the line is proportional to the total flux through the reaction over the course of a simulation.	75
4-1	Measurement-model comparison for 8:2 FTOH concentrations at two remote and one urban location. The gray boxes represent the median and the lower and upper quartiles of the measurement data, with whiskers extending to the full range of the measurements. The blue boxes represent the model range between maximum and minimum emissions scenarios.	88
4-2	Measurement-model comparison for PFOA deposition for 2004 (first bars) and 2005 (second bars) at four Canadian ice caps. The gray boxes represent the measurement uncertainty, with error bars representing the error from comparing a point measurement to model grid-box. The blue boxes represent the model range between maximum and minimum emissions scenarios.	89

4-3	Measurement-model comparison for PFNA deposition for 2004 (first bars) and 2005 (second bars) at four Canadian ice caps. The gray boxes represent the measurement uncertainty, with error bars representing the error from comparing a point measurement to model grid-box. The blue boxes represent the model range between maximum and minimum emissions scenarios, with the blue error bar representing the perfluorinated aldehyde hydration sensitivity test.	90
4-4	Spatial distribution of PFOA deposition (kg/yr) in each GEOS-Chem grid-box.	91
4-5	Spatial distribution of PFNA deposition (kg/yr) in each GEOS-Chem grid-box.	92
4-6	Time series of annual total Arctic deposition of PFOA (gray) and PFNA (blue). Orange mark corresponds to Wania [66] estimate and red mark corresponds to Wallington [61].	93
4-7	Time series of annual total Arctic deposition of PFOA (gray) and PFNA (blue).	94
4-8	Spatial distribution of the PFOA fraction of total deposition of fluorinated species.	95
4-9	Spatial distribution of the PFNA fraction of total deposition of fluorinated species.	96

List of Tables

2.1	Uncertainty of physicochemical properties in GEOS-Chem PAH simulations (means and standard deviations of normal distributions) . . .	44
2.2	Physicochemical parameter data for PHE	48
2.3	Physicochemical parameter data for PYR	49
2.4	Physicochemical parameter data for BaP	50
2.5	Site info, annual average total concentrations (and ± 1 standard deviation of observational error) for PAH observation sites.	51
2.6	Contributions of leading physicochemical property and regional emission uncertainties to overall uncertainty in Northern Hemisphere (NH) and Arctic concentrations of PHE (i and ii), PYR (iii and iv), and BaP (v and vi). Contributions are expressed as percentages of total uncertainty accounted for by each individual parameter rounded to the nearest percentage point. Parameters contributing $<1\%$ are not included.	52
3.1	List of reactions.	72
3.2	Case environment conditions. Photochemical concentrations in cm^{-3} , temperatures in K	73
3.3	Fractional yield uncertainty contributions of rate constants (%) . . .	73

Chapter 1

Introduction

Persistent organic pollutants (POPs) are environmental contaminants which are characterized by their persistence in some part of the environment, due to slow degradation by chemical or biological processes. POPs often bioaccumulate, are toxic, and are often significantly or entirely released to the environment by human activities. In this thesis, I study two sets of compounds that can be classified as POPs: polycyclic aromatic hydrocarbons (PAHs) and perfluorocarboxylic acids (PFCAs). PAHs are by-products of burning and therefore have important anthropogenic sources in the combustion of fuels, biomass, etc. PFCAs and their atmospheric precursors are used in making firefighting foams, non-stick coatings, and other surfactant applications.

1.1 Motivation for studying PAHs and PFCAs in the atmosphere

Polycyclic aromatic hydrocarbons (PAHs) are mutagenic and carcinogenic environmental contaminants[6]. PAHs travel through the atmosphere across national boundaries and are found in regions such as the Arctic far from sources [26, 38, 25, 28], where they are found in the tissues of biota. PAH concentrations are higher than many POPs by orders of magnitude. PAHs are regulated internationally as POPs, via the Convention on Long-Range Trans-boundary Air Pollution (CLRTAP) [59]. Despite

regulatory efforts, PAHs continue to be transported via the atmosphere to the Arctic. Uncertainty surrounding pathways by which PAHs reach remote locations has been the subject of recent research, especially concerning their gas-particle partitioning and oxidation. The pathways by which PAHs reach the Arctic have been studied with numerical models of varying complexity [50, 67, 48, 62, 34, 19, 21]. However, our understanding of these pathways is limited by substantial uncertainty associated with the physicochemical properties (including reaction rate constants, partition coefficients and energies of phase change) that determine the atmospheric fate of PAHs. Some physicochemical properties governing PAH behavior, such as oxidation rate constants and black carbon partition coefficients, are poorly constrained by measurements or have not been measured directly [8, 36, 53]. For some smaller PAHs, physicochemical parameters important to their atmospheric fate have been relatively more studied than for the larger PAHs. Even for these small PAHs, measurements of physicochemical properties can differ by more than a factor of two [36]. Limited knowledge of- and uncertainty associated with- emissions sources also contributes to uncertainty in atmospheric transport, as emissions factors for some processes can vary by orders of magnitude [76]. Model uncertainty has been studied for multimedia fate models of persistent organics [17, 47, 41]. Multimedia model analyses have found that chemical properties have a larger influence on persistence and long-range transport potential than model parameters such as spatial scales, media heights/depths, and land and water surface fractions [17]. Detailed Monte Carlo-type analyses have been performed for multimedia models, finding that emissions and degradation constants were the most influential sources of uncertainty in DDT concentrations [47] and that partition coefficients and reaction rate constants accounted for more than half of the uncertainty in mercury concentrations in the air and the surface ocean [44]. It is my goal in Chapter 2 of this thesis to characterize the parametric uncertainty involved with modeling atmospheric PAHs.

Perfluorocarboxylic acids (PFCAs) are environmental contaminants that are highly persistent, bio-accumulative [40, 39, 13], and have been detected along with their atmospheric precursors far from emissions sources [73, 54, 56] in snow [71], precipitation

[49], and biota [27]. Of particular environmental interest are the long-chain PFCA (lcPFCA) homologues such as PFOA (8-Carbon chain), due to the increase of detrimental effects with chain length [40, 39, 13]. Reducing lcPFCA emissions has been the intent of policy actions due to their health effects [60], resulting in decreasing direct emissions globally. At the same time, emissions of atmospheric precursors of PFCAs are rising [64], leading to an increasing indirect source of PFCAs to the environment. These precursors, including fluorotelomer alcohols (FTOHs), react with atmospheric photochemical species [15] in a multi-stage process to form PFCAs [75]. This mechanism follows the degradation of 8:2 fluorotelomer (FT) products, which are the most commonly emitted PFCA precursors [64], to form FT-aldehyde and further intermediate and stable end products including PFOA and other PFCAs. The FT-aldehyde can be oxidized by OH or photolyzed to form peroxy and acylperoxy radicals. These radicals react with NO, NO₂, RO₂, and HO₂ to form intermediates which can again be radicalized by OH and ultraviolet light, with further radical reactions leading to stable PFCAs or intermediates with reduced chain length. However, the importance of precursor emissions as an indirect source of lcPFCAs to the environment is uncertain. Estimated yields of PFCAs from precursors can vary based on differences in the formation mechanism assumed, quantitative uncertainty in reaction rate constants, and ambient concentrations of other atmospheric species.

Previous studies have estimated yields of lcPFCAs from the degradation of FTOHs in the atmosphere [72, 61]. However, studies have indicated that other emitted atmospheric precursors exist in the form of other fluorotelomer compounds [75, 64, 65, 74, 9]. Rate coefficients for the reactions in the PFCA formation mechanism are uncertain, affecting estimated yields. The atmospheric formation of PFCAs depends on reactions of fluorinated intermediates [68, 12] with commonly studied photochemical species, such as HO_x and NO_x species, as well as ultraviolet light. These species vary greatly over different environments in the atmosphere, affecting the quantity of lcPFCA produced. Until recently, the chemical pathways that lead to PFCA formation were incompletely characterized, and even currently many of the radical reactions that lead to PFCAs have not been measured directly. Quantifying the uncertainty in

this chemistry of formation is therefore an important step toward better understanding atmospheric PFCA formation.

Modeling studies have used degradation mechanisms of differing complexities to estimate the atmospheric production of PFCAs, and these differing mechanisms lead to quantitatively different yields of lcPFCAs under differing atmospheric conditions. [61] simulated the atmospheric degradation of 8:2 FTOHs using the IMPACT atmospheric chemistry model, finding that PFOA yields ranged from 1-10% depending on location and time. Yarwood et al. [72] used a higher resolution atmospheric chemistry model over North America to estimate that degradation yielded approximately 6% PFOA on average, and much less than 1% PFNA. Schenker et al. [46], using a global-scale multispecies mass-balance model with simplified chemistry, found that precursor transport and degradation could contribute to perfluorocarboxylates observed in the Arctic, and that rate constant uncertainty was an important contributor to uncertainty in their results [46]. In Chapter 3, I investigate PFCA formation with the most complete degradation mechanism to date to our knowledge, including the reactions presented in the studies of Wallington et al. [61] and Yarwood et al. [72], and the review of Young and Mabury [75]. I quantitatively estimate the influence of uncertainty in rate coefficients for calculations of PFCA yields and examine the influence of different atmospheric chemical conditions on upper-limit PFCA formation.

From Chapter 3, it is apparent that the connection between chemistry, transport, and deposition of PFCAs, their precursors, and intermediates in their formation, is important to the quantity of PFCA formed in the atmosphere as well as deposited to remote locations such as the Arctic. Atmospheric chemical transport models are therefore an important tool to quantifying formation and fate of PFCAs in the atmosphere. In Chapter 4, I present results from newly developed simulations of atmospheric PFCA formation and fate using the global CTM GEOS-Chem. Simulating the chemistry studied in Chapter 3 for the degradation of the emitted PFCA precursors 8:2 FTOH and fluorotelomer iodide (FTI), as well as deposition and transport of the precursors, intermediates and end-products of the degradation chemistry. I find again that yields of lcPFCAs vary greatly by geographic location, and that the annual

response to increasing emissions is variable. I compare the model outputs to remote deposition and concentration measurements and estimate the indirect atmospheric source of PFCAs globally and to the Arctic.

1.2 Main tools

Throughout this thesis I will be making use of a pair of tools for studying the atmospheric fates of PAHs and PFCAs: the GEOS-Chem atmospheric chemical transport model and polynomial chaos expansions. GEOS-Chem is a model which accounts for emissions, photochemistry, deposition, and atmospheric transport of chemical species of interest in the atmosphere. Polynomial chaos expansions (PCE) are used to simplify complicated and computationally expensive models such as GEOS-Chem for the purposes of uncertainty analysis.

1.2.1 GEOS-Chem atmospheric chemical transport model

GEOS-Chem is a chemical transport model (CTM) which uses prescribed reanalysis meteorology to calculate the transport of chemical species in the atmosphere. On top of this transport, GEOS-Chem simulates the chemical reactions, photolysis, deposition, and phase partitioning of the chemical species of interest. GEOS-Chem is used for a variety of atmospheric chemistry applications, including photochemical air pollution, mercury, PAHs, and now PFCAs, among others. It is widely used because of its flexibility in simulating a variety of chemistries at a range of spatial scales, from coarser $4^{\circ}\times 5^{\circ}$ resolution down to less than 1° resolution in nested grid applications. GEOS-Chem's ability use actual meteorology and a fine resolution on a global scale make it ideal for comparisons to measurements in remote locations, which is particularly important for POPs research. Throughout this work, I use GEOS-Chem in a variety of applications, but consistently at $4^{\circ}\times 5^{\circ}$ resolution. While for conventional air quality studies this would be considered coarse resolution, in POPs applications, this is considered fine scale. In Chapters 2 and 4, we choose this resolution as a balance between computational efficiency and the ability to differentiate the measurement

sites to which we compare GEOS-Chem. In Chapter 3, we choose this resolution to balance capturing the variability in photochemical environment with computational efficiency.

1.2.2 Polynomial chaos expansions for uncertainty analysis

PAHs have been studied using fine-scale models at both the global and regional scales. Through comparison to spatially and temporally fine-scale measurements, these studies show that highly spatially resolved models can be useful in predicting the pattern of exposure to PAHs, an important factor for human health impacts. While multimedia models are computationally efficient and thus can quantitatively examine relative influences of parameters on uncertainty, they lack the spatial resolution and ability that CTMs possess to resolve the episodic nature of atmospheric transport. Monte Carlo-type methods like those used for multimedia models can be prohibitively computationally expensive for more finely spatially resolved models. Individual simulations run with complex atmospheric CTMs such as GEOS-Chem can require hours to days of computational time, leading to years for the full Monte Carlo analysis. Thus, first-order parameter sensitivity tests are often used to characterize uncertainty in spatially resolved models. One previous study reported quantitative estimates of the relative importance of physicochemical parameter uncertainty and emissions uncertainty in PCB153 and α -HCH simulations by the large-scale, spatially-resolved ($15^\circ \times 15^\circ$) BETR Research model using a first-order error propagation method. Though first-order error propagation methods are computationally cheaper than Monte Carlo analysis, they do not directly quantify the effect of parameter uncertainty interactions. Polynomial chaos expansion (PCE)-based methods can greatly reduce the computational cost of uncertainty propagation for CTMs compared to Monte Carlo methods, while approximating the resulting uncertainty distributions more closely than first-order methods by extending to higher order. PCE-based methods quantify the relative importance of each parameter, as well as account for their interactions in the model system, a significant advantage over traditional model parameter sensitivity tests. They also provide computational efficiency while retaining

the spatial and temporal fidelity of CTMs.

We calculate the uncertainties for model outputs using polynomial chaos expansion (PCE) methods to propagate uncertainty from rate constants and physicochemical properties to outputs calculated in both GEOS-Chem and box-model simulations. PCE methods are used to create a polynomial representation of the model, which can propagate uncertainty in model inputs to model outputs at reduced computational expense. While being computationally less expensive, the polynomial representation is able to represent non-linear responses of the model and interactions between the effects of changing multiple input parameters [58, 37, 11]. The PC estimator is composed of orthogonal polynomials of the form

$$\eta(\zeta) = \alpha_0 + \sum_{j=1}^d \sum_{k=1}^M \alpha_{j,k} H_j(\zeta_k) + \sum_{k=1}^{M-1} \sum_{l=k+1}^M \beta_{k,l} H_1(\zeta_k) H_1(\zeta_l) + \dots + \text{Order}(d > 2) \quad (1.1)$$

where the estimator η of degree d is a function of the polynomials H_j of order j , the M variables ζ_k representing model inputs, the expansion coefficients $\alpha_{j,k}$ and $\beta_{k,l}$, and higher order coefficients. Not shown in the equation are cross terms of degree >2 , which include the product of up to d Hermite polynomials of different variables, analogous to the second order cross terms shown. In the following studies, we truncate the polynomial after second or third order to further reduce computational cost. To calculate the expansion coefficients, a model run at a unique set of inputs is performed for each term in the equation [57], with the inputs for the model runs for each degree's terms being the values corresponding to the roots of the next degree's polynomials. The outputs of these model runs and the corresponding sets of input values are used to set up a system of equations to solve for the expansion coefficients [37]. We use the polynomial estimator to directly calculate the parameters of the uncertainty distributions of the model outputs of interest without relying on Monte Carlo methods [37]. We also calculate the fraction of the variance in model outputs contributed by each rate constant or physicochemical parameter using the expansion coefficients [37, 11].

1.3 Overview

In Chapter 2, I study the uncertainty in GEOS-Chem PAH simulations that stems from uncertain model inputs such as physicochemical properties and emissions estimates. Using PCE, I quantify uncertainty, identify the leading contributors to uncertainty, and use measurements along with uncertainty information to better constrain the uncertain model inputs.

In Chapter 3, I investigate atmospheric PFCA formation from emitted precursors using a box model driven by GEOS-Chem outputs of photochemical species such as HO_x and NO_x , to quantify the variability in PFCA yields in different atmospheric environments, and using PCE, to quantify uncertainty in these yields.

In Chapter 4, I introduce simulations of PFCA formation in GEOS-Chem itself, accounting for emissions of precursors, the chemistry that leads to PFCAs, and the transport and deposition of all of the products of the chemistry. I compare simulations to remote measurements of concentrations and deposition and calculate global and Arctic fluxes of PFCAs due to atmospheric formation and transport.

Chapter 5 includes concluding remarks and further discussion.

Chapter 2

Quantitative assessment of parametric uncertainty in Northern Hemisphere PAH concentrations

Adapted with permission from: Quantitative Assessment of Parametric Uncertainty in Northern Hemisphere PAH Concentrations; Colin P. Thackray, Carey L. Friedman, Yanxu Zhang, and Noelle E. Selin *Environmental Science & Technology*, 2015, 49 (15), 9185-9193 DOI: 10.1021/acs.est.5b01823

Copyright (2015) American Chemical Society

2.1 Abstract

We quantitatively examine the relative importance of uncertainty in emissions and physicochemical properties (including reaction rate constants) to Northern Hemisphere (NH) and Arctic polycyclic aromatic hydrocarbon (PAH) concentrations, using a computationally-efficient numerical uncertainty technique applied to the global-scale chemical transport model GEOS-Chem. Using polynomial chaos (PC) methods, we propagate uncertainties in physicochemical properties and emissions for the PAHs benzo[a]pyrene, pyrene and phenanthrene to simulated spatially-resolved concentration uncertainties. We find that the leading contributors to parametric uncertainty in

simulated concentrations are the black carbon-air partition coefficient and oxidation rate constant for benzo[a]pyrene, and the oxidation rate constants for phenanthrene and pyrene. NH geometric average concentrations are more sensitive to uncertainty in the atmospheric lifetime than to emissions rate. We use the PC expansions and measurement data to constrain parameter uncertainty distributions to observations. This narrows a priori parameter uncertainty distributions for phenanthrene and pyrene, and leads to higher values for OH oxidation rate constants and lower values for European PHE emission rates.

2.2 Introduction

Polycyclic aromatic hydrocarbons (PAHs) are mutagenic and carcinogenic environmental contaminants [6]. As persistent organic pollutants (POPs) that are transported through the atmosphere across national boundaries after emission, PAHs are regulated internationally by the Convention on Long-Range Trans-boundary Air Pollution (CLRTAP) [59]. Despite regulatory efforts, PAHs continue to be transported via the atmosphere to the Arctic [26, 38, 25, 28], far from source regions. In this study, we quantitatively examine the relative importance of emissions and physicochemical parametric uncertainty to Northern Hemispheric (NH) and Arctic PAH concentrations, using efficient numerical uncertainty techniques applied to the global-scale chemical transport model (CTM) GEOS-Chem.

The pathways by which PAHs reach the Arctic have been studied with numerical models of varying complexity [50, 67, 48, 62, 34, 19, 21]. However, our understanding of these pathways is limited by substantial uncertainty associated with the physicochemical parameters (including reaction rate constants, partition coefficients and energies of phase change) that govern the atmospheric fate of PAHs. Some physicochemical parameters representing PAH behavior, such as oxidation rate constants and black carbon partition coefficients, are poorly constrained by measurements or several have not been measured directly [8, 36, 53]. For some PAHs, e.g. phenanthrene (PHE; three ring), physicochemical parameters important to their atmospheric fate

have been relatively more studied than for the larger PAHs like benzo[a]pyrene (BaP; five ring) and pyrene (PYR; four ring). Even for PHE, measurements of physico-chemical parameters can differ by more than a factor of two [36]. Limited knowledge of emissions sources and associated uncertainty also contributes to uncertainty in atmospheric transport, as emissions factors for some processes (e.g. waste incineration, biomass burning) can vary by orders of magnitude [76].

Model uncertainty has been studied for multimedia fate models of persistent organics [17, 47, 41]. Multimedia model analyses have found that chemical properties have a larger influence on persistence and long-range transport potential than model parameters such as spatial scales, media heights/depths, and land and water surface fractions [17]. Detailed Monte Carlo analyses have been performed for multimedia models, finding that emissions and degradation constants were the most influential sources of uncertainty in DDT concentrations [47] and that partition coefficients and reaction rate constants accounted for more than half of the uncertainty in mercury concentrations in air and the surface ocean [44].

PAHs have been studied using finer-scale models at both the global and regional scales [50, 19, 21, 22, 20]. Through comparison to spatially and temporally fine-scale measurements, these studies show that highly spatially resolved models can be useful in predicting the pattern of exposure to PAHs, an important factor for human health impacts. While multimedia models are computationally efficient and thus can quantitatively examine relative influences of parameters on uncertainty, they lack the spatial resolution and ability that CTMs possess to resolve the episodic nature of atmospheric transport.

Monte Carlo-type methods like those used for multimedia models [47] can be prohibitively computationally expensive for more finely spatially resolved models, as they require on the order of thousands of samples for detailed analyses. Individual simulations run with complex atmospheric CTMs such as GEOS-Chem can require hours to days of computational time, leading to years for the full Monte Carlo analysis. Thus, first-order parameter sensitivity tests are often used to characterize uncertainty in spatially resolved models [19, 20, 69].

One previous study [69] reported quantitative estimates of the relative importance of physicochemical parameter uncertainty and emissions uncertainty in PCB153 and α -HCH simulations by the large-scale, spatially-resolved ($15^\circ \times 15^\circ$) BETR Research model using a first-order error propagation method. Though first-order error propagation methods are computationally cheaper than Monte Carlo analysis, they do not directly quantify the effect of parameter uncertainty interactions. Polynomial chaos (PC)-based methods can greatly reduce the computational cost of uncertainty propagation for CTMs compared to Monte Carlo methods, while approximating the resulting uncertainty distributions more closely than first-order methods by extending to higher order. Parametric uncertainty in complex chemical mechanisms has been quantified using PC methods in a number of applications [43, 30, 37, 11]. PC-based methods quantify the relative importance of each parameter, as well as account for their interactions in the model system, a significant advantage over traditional model parameter sensitivity tests. They also provide computational efficiency while retaining the spatial and temporal fidelity of CTMs.

We present here a first application of PC-based methods to a global atmospheric CTM of POPs. We use this analysis to quantify the contributions of emissions and physicochemical parameter uncertainty to NH- and Arctic-average concentrations of PHE, PYR, and BaP. We then combine the results of our PC analysis with measurements from long-term observation sites to constrain the values of these parameters.

2.3 Methods

To quantify uncertainty in the GEOS-Chem PAH simulations, we compare simulated concentrations and associated uncertainties to measurements at non-urban sites, and use these measurements and their uncertainties in a Bayesian analysis to constrain the probability distributions of the physicochemical parameters. Throughout this work we will refer to model "parametric uncertainty", which is the uncertainty in simulated concentrations resulting directly from the uncertainty in the model input parameters; i.e. physicochemical properties and emissions magnitudes.

2.3.1 GEOS-Chem Model

The simulations we assess in this study are carried out using the GEOS-Chem PAH chemical transport model [19]. This model has been used in previous studies to simulate long-range atmospheric transport of PAHs and has allowed comparison to measurements where it has been able to resolve meteorologically-driven episodic high-concentration events [19]. Evaluation of the model against measurements in both mid-latitudes and the Arctic, and traditional sensitivity tests have been conducted previously; we refer the reader to the referenced papers for a detailed assessment of model performance [19, 21]. Here, we briefly describe major features of the model, including meteorology, emissions, chemistry, and gas-particle partitioning. GEOS-Chem uses assimilated meteorology from the NASA Goddard Earth Observing System's GEOS-5 dataset at a temporal resolution of 6 hours, a horizontal resolution of $0.5^\circ \times 0.667^\circ$ re-gridded to $4^\circ \times 5^\circ$ for computational efficiency, and 47 levels vertically. The simulations for this study were run for the years 2006-2008. PAH emissions in the model come from the inventory of Zhang and Tao [76], which represents annual emissions from the year 2004, is resolved on the national scale, and includes details for individual sectors and PAHs but is not time-resolved, meaning the emissions are not seasonally or annually varying. Emissions are discussed in more detail in following sections. Each model run begins with a "spin-up" period of one simulated year to negate the transient effects of initial conditions.

Upon emission, the model partitions PAHs between the gas and aerosol phases using a black carbon-air partition coefficient (K_{BC}) to represent partitioning to black carbon (BC) aerosol and an octanol-air partition coefficient (K_{OA}) to represent partitioning to organic carbon (OC). The overall gas-particle partitioning is governed by a dual OC adsorption and BC adsorption model [19] based on the Dachs-Eisenreich [14] equation. Both OC and BC concentrations are prescribed as monthly averages in the PAH simulations, pre-calculated from full chemistry GEOS-Chem simulations [62, 7] for computational efficiency. Gas-particle partitioning is re-calculated at each chemistry time step of GEOS-Chem (60 min). The effect of using this coarse time

resolution of prescribed particle concentrations was found to be small compared to the parametric uncertainties discussed below [21]. Each of these partition coefficients' temperature dependence is determined by an internal energy of phase change according to the van't Hoff relationship. These internal energies are governed by enthalpies of phase change. The enthalpy of vaporization ΔH_{vap} is the uncertain parameter that determines the sensitivity of particle partitioning to changing temperature, while the enthalpy of solvation in liquid water ΔH_{sol} in combination with ΔH_{vap} determines that of wet deposition.

We simulate the oxidation of gas phase PAHs by reaction with hydroxyl radicals (OH). Monthly average OH concentrations are prescribed by a GEOS-Chem full chemistry simulation [4] with a daily cycle overlaid on these monthly averages. PAH reaction with OH is represented by a second order reaction with reaction rate constant k_{OH} . On-particle oxidation by ozone is simulated using the parametrization of Kahan et al [31]. Both gas- and particle-phase PAHs undergo wet deposition in the simulations. Gas-phase PAH is scavenged by liquid water according to the air-water partitioning coefficient K_{AW} , which is temperature dependent according to ΔH_{AW} (a combination of ΔH_{sol} and ΔH_{vap}) following the van't Hoff relationship. Dry deposition for gas-phase PAH is simulated according to Wang et al. [63], with lipophilic uptake scaled by the K_{OA} [19]. A complete evaluation of GEOS-Chem simulations of PAHs can be found in the original work by Friedman and Selin [19]. The seven uncertain physicochemical parameters mentioned above are included in our analysis for each PAH.

2.3.2 Polynomial chaos

The PC-based estimator uses orthogonal polynomials to approximate GEOS-Chem model output as a function of model inputs. The polynomial expansion of the model output to be estimated takes the form

$$\eta(\xi) = \alpha_0 + \sum_{j=1}^d \sum_{k=1}^M \alpha_{j,k} H_j(\xi_k) + \sum_{k=1}^{M-1} \sum_{l=k+1}^M \beta_{k,l} H_1(\xi_k) H_1(\xi_l) + \dots + Order(d) \quad (2.1)$$

where the estimator η of degree d is a function of the polynomials H_j of order j , the M variables ξ_k representing model inputs, the expansion coefficients $\alpha_{j,k}$ and $\beta_{k,l}$, and higher order coefficients. The terms not shown in the equation are cross terms of degree greater than two, which include the product of up to d Hermite polynomials of different variables, analogous to the second order cross terms shown. In this study, we truncate the polynomial after third order. To obtain the expansion coefficients, one model run at a unique set of inputs is performed for each term in equation 2.1 [57]. The set of inputs for the model runs for each degree's terms are the values corresponding to the roots of the next degree's polynomials. The outputs of these model runs and the corresponding sets of input values are used to set up a system of equations to solve for the expansion coefficients [37]. Further description, along with validation, of the PC expansion can be found in Chapter 1. We use the polynomial estimator to directly infer properties of the uncertainty distribution of model output (in this case total (gas plus particulate phase) PAH mass concentration) without relying on Monte Carlo methods, which is accomplished using the analytical forms of the mean, variance and skewness from the polynomial coefficients [37]. We also calculate the portion of the total output variance contributed by each input parameter using the expansion coefficients [37, 11].

2.3.3 Physicochemical parameter uncertainties

We conduct an extensive review of the literature for experimentally determined values of each of seven uncertain physicochemical parameters for the three PAHs investigated in this study, and construct probability distributions based on the available data (summarized in Tables 2.2-2.4). The distributions (Table 2.5 and discussed below), are for the parameters that most directly affect the simulated atmospheric fate and transport of the PAHs based on previously-conducted traditional model sensitivity testing [19]. Model processes that are sources of uncertainty for all chemicals (including non-POPs) simulated by GEOS-Chem, such as advection and wet deposition schemes, are not the focus of this study.

Partition coefficients (air-water: K_{AW} , black carbon-air: K_{BC} , octanol-air: K_{OA}):

Since the partition coefficients used in the model are experimentally determined and reported in log form, we estimate their uncertainty distributions as normal distributions of the log values, with the means and standard deviations derived from literature values (see SI for details and references). K_{BC} , which describes the fraction of PAH found in the BC phase given an amount of BC particulate matter, is the combination of K_{AW} and the BC-water partition coefficient ($K_{BC-water}$) [3],

$$\log(K_{BC}) = -\log(K_{AW}) + \log(K_{BC-water}) \quad (2.2)$$

where $K_{BC-water}$ gives the ratio of concentrations of PAH in the BC particulate phase to dissolved PAH at equilibrium. Since K_{BC} itself is not an independent parameter due to its relationship to K_{AW} , we use the independent $K_{BC-water}$ instead as the uncertain parameter for this study.

Enthalpies of phase change (ΔH_{vap} and ΔH_{sol}): We estimate the uncertainty distributions for the enthalpy of vaporization (ΔH_{vap}) and the enthalpy of solvation (ΔH_{sol}) for PHE, PYR and BaP as normal distributions with the means and standard deviations of a collection of literature values of ΔH_{vap} or ΔH_{sol} for each PAH (see SI for details and references).

On-particle ozone oxidation rate constant (k_{O_3}): For all three PAHs, we use the reported "A" and "B" kinetic parameter values and their uncertainties from Kahan et al. [31] as model inputs. Across all atmospheric ozone concentrations, the B-parameter dominates the contribution to uncertainty in k_{O_3} , so we neglect A-parameter uncertainty in our analysis.

OH oxidation rate constant (k_{OH}): For PHE, we estimate the uncertainty distribution from three literature values and their associated uncertainties [8, 33, 2]. The mean value of the normal uncertainty distribution is estimated by the uncertainty-weighted mean of these three values, and the standard deviation of the distribution is estimated by the standard deviation of the weighted mean.

While there is no literature value for BaP's or PYR's k_{OH} , values can be obtained from the Atmospheric Oxidation Program software AOPWIN, which uses an

ionization potential-activity relationship [5],

$$\ln(k_{OH}) = -4.345 - 2.494(IP) \quad (2.3)$$

where k_{OH} has units of $\text{cm}^3 \text{ molec}^{-1} \text{ s}^{-1}$ and IP is the ionization potential in units of eV. We use the mean and standard deviation of the National Institute of Standards and Technology collection of reported ionization potentials for BaP [42] to estimate a normal distribution that results in a log-normal distribution of IP-derived k_{OH} values. Similarly, for PYR we use the mean and standard deviation of the collection of reported PYR IPs [32] to estimate the uncertainty distribution for PYR's k_{OH} .

2.3.4 Regional emissions uncertainties

Emissions uncertainty results from uncertainties in both emission activities (quantity of a given type of emitting process) and emission factors (PAH emission quantity per activity). The total PAH emission E due to a process i can be divided into those two elements:

$$E_i = A_i F_i \quad (2.4)$$

where A_i is the emissions activity of process i and F_i is the emission factor for that process. F_i can be uncertain to a much larger degree than A_i [76] because the conditions under which each emitting process is carried out in reality are highly varying but summarized by a single value. Measurements of F_i of the same process by different experimenters can yield orders of magnitude differences [76]. For example, F_i associated with diesel fuel in the transport sector will depend on such factors as the type of fuel burned, type of engine burning the fuel, and temperature and condition of the engine. PAH emissions processes with the largest uncertainties in F_i include primary aluminum production, use of traffic gasoline, diesel, and kerosene, industrial coal burning, and non-transport petroleum combustion [76].

Given that there are distinct source contributions to PAH emissions and their uncertainties in different regions of the globe, we define discrete emissions regions, and

calculate an a priori probability distribution for the total emissions of each region. We choose the regions of North America, Europe, South Asia, East Asia and Africa because of the large magnitude of emissions (South Asia, East Asia, Africa), and proximity to the Arctic (North America and Europe). We estimate the uncertainty distribution of total emissions of each region using Monte Carlo sampling over each country's A_i and the F_i uncertainty distributions [76] and assume that the spatial distribution of emissions within each region remains fixed. Regional emission distributions are then used as input parameters, along with physicochemical parameters, in the above-described PC analysis.

2.3.5 In-situ observations

We use observed annual average total (gas+particulate) BaP, PYR, and PHE concentrations from each of 10 sites monitored by the Co-operative Programme for Monitoring and Evaluation of the Long-range Transmission of Air Pollutants in Europe (EMEP), Integrated Atmospheric Deposition Network (IADN), and Environment Canada (EC) observation networks in the Northern Hemisphere (NH) for comparison to model values. All observations were collected at land-based non-urban sites using high-volume air samplers. Particle-bound PAHs were collected on glass fibre filters, and volatile PAHs were adsorbed to polyurethane foam (PUF) plugs. Spatial coverage includes the Great Lakes, Northern Europe, and two Arctic sites. Site locations, concentrations and references are summarized in Table 2.6, and are the same sites used for model-measurement comparison by Friedman and Selin [19].

For site-by-site comparison to simulated concentrations, we calculate observational errors following Chen and Prinn [10]. The observational error for comparison to a model grid box accounts for statistical representativeness (accounting for some stations' non-continuous sampling), analytical method precision error, site intercalibration error, and spatial mismatch error (i.e. a single point's representativeness of the whole grid-box). These errors (see Table 2.6) represent the variability in observed values that is impossible to capture with any model, and are thus separate from model uncertainty. These errors range from $\pm 25\%$ to a factor of 3, depending

on the measurement site and the PAH in question.

2.3.6 Constraint of physicochemical parameters by observations

Using the annual average measurements outlined above, and PC-estimated concentrations based on annual average model output, we constrain the physicochemical parameter uncertainty distributions by Bayesian inference, combining information from observations and a priori parameter uncertainties. We compare 1) the PC polynomial-estimated concentration in the model grid box encompassing a measurement location for a given set of physicochemical and emissions parameter values to 2) the observed concentration at the same location. By mapping the predicted concentrations as a function of the uncertain parameters using the PC estimator, we define a weighted least-squares cost function of the form:

$$\chi(\xi)^2 = \sum_{i=1}^N \left(\frac{Y_i - \eta_i(\xi)}{\sigma_i} \right)^2 \quad (2.5)$$

where summation is over the N measurement locations, Y_i is the observed value at a particular site, $\eta_i(\xi)$ is the polynomial estimate at parameter values ξ , and σ_i is the total "observation errors" from above at measurement site i . With the least-squares comparison above, the likelihood function $P(Y|\xi)$ is related to the cost function via

$$P(Y|\xi) \propto e^{-K(\xi)^2} \quad (2.6)$$

This makes use of the PC estimators and the site measurements and their errors to estimate the likelihood of observing the concentrations Y as a function of the parameter values ξ . To update the a priori uncertainty distributions, we use Bayes' rule for the a posteriori distribution $P(\xi|Y)$:

$$P(\xi|Y) \propto P(\xi)P(Y|\xi) \quad (2.7)$$

where $P(\xi)$ is the prior uncertainty distribution. This results in a description of the relative probabilities of each physicochemical parameter value, given the available constraining measurements.

2.4 Results

We calculate polynomial estimators as described above, and evaluate their predicted log-concentrations against independent full GEOS-Chem model runs. Over the parameter space covered by the physicochemical property uncertainty distributions, the polynomial estimator matches the validation data-set with r^2 greater than 0.99 for all three PAHs. We use the polynomial estimators to calculate model uncertainty distributions for NH and Arctic (above 66°N) surface concentration geometric averages for annual and Northern Hemisphere winter (DJF) and summer (JJA) periods for all three PAHs, attribute fractions of this uncertainty to individual model parameters, and constrain parameter uncertainty distributions using observation site data.

2.4.1 Comparison to measurements

Figure 2-1 shows a comparison of monthly average concentrations simulated using the PC-based estimator and associated parametric uncertainties to measured average concentrations and measurement uncertainties for non-urban sites for each PAH. The simulations capture the measurements within the $\pm 2\sigma$ parametric uncertainty interval for all three PAHs, with PYR and BaP capturing the measurement means within the $\pm\sigma$ interval.

Simulated PHE concentrations show agreement with measurements during the winter-spring and summer-fall transitions, but measured means are higher than simulated during JJA and lower during DJF [19]. In the summer, the measured mean falls within the $\pm\sigma$ bounds of the model, but during the winter months (Nov, Dec, Jan, Feb), the measured concentrations fall between the $-\sigma$ and -2σ model values. This discrepancy could be due to unresolved seasonality of emissions, or secondary sources which are not represented in the simulations, but have been tested and discussed pre-

viously [21]. PYR simulated concentrations are lower than observed concentrations for all except the winter months. The observed values do, however, fall into the $\pm\sigma$ range of the model uncertainty distribution for all months. BaP simulated concentrations have the highest parametric uncertainty, and the observed concentrations fall into the $\pm\sigma$ range of the model for all months of the year, with the simulated seasonal cycle following the observed cycle closely. Northern Hemisphere and Arctic model uncertainty in concentration Figure 2-3 shows model parametric uncertainty distributions for BaP, PYR and PHE, for both NH and Arctic average concentrations, and for annual, winter, and summer temporal averages. Across all three PAHs, JJA average simulated concentrations are lower with higher uncertainty than DJF averages. PHE concentrations have the least parametric uncertainty, with a range (95% confidence interval) spanning approximately one order of magnitude for annual, summer, and winter averages. PYR and BaP parametric uncertainty ranges during the summer span more than two orders of magnitude, and close to an order of magnitude during the winter.

In the Arctic, parametric uncertainty is at its lowest for all three PAHs during the winter, when there is little to no sunlight to drive photochemical oxidation. Average concentrations of PAHs are highest during the winter, and lowest during the summer in the Arctic because of the presence of OH for oxidation, and this relative abundance of OH also drives the sensitivity of the PAH concentrations to oxidation rate constant uncertainty. The seasonal difference in the Arctic average PAH concentration is more pronounced than the NH average, with summer-winter differences for all three PAHs of more than three orders of magnitude.

2.4.2 Contributors to model parametric uncertainty

The important sources of model parametric uncertainty are substantially different between NH and Arctic average concentrations, and across the three PAHs. Table 2.6 shows the fractional contribution of leading parameters to the total resulting model parametric concentration uncertainty for PHE, PYR, and BaP. At the hemispheric scale, PHE concentration parametric uncertainty is driven year-round by uncertainty

in the oxidation rate constant. Since PHE is mostly in the gas phase (90%-100% [19]), uncertainty in its gas-phase lifetime is the most important contributor to parametric uncertainty in the NH average simulated concentrations. In the Arctic average, however, uncertainty in European emissions gains importance, contributing close to a third of the parametric uncertainty annually and 64% in the winter. The relative importance of emissions and reduced importance of oxidation rate constant uncertainty during Arctic winter is due to the lack of atmospheric OH radicals. During the summer, European emissions uncertainty remains a significant secondary contributor, but k_{OH} uncertainty makes up the largest fraction of the total for the model.

The contributors of PYR parametric concentration uncertainty follow a similar pattern to those of PHE. Because of the large uncertainty in the oxidation rate constant for PYR (see Table 2.5) and the fact that >50% of atmospheric PYR is in the gas phase [19], the parametric concentration uncertainty in the NH annual average is dominated by uncertainty in k_{OH} . Like for PHE, the second-most important contributor to parametric uncertainty is European emissions. BaP has the most varied contributions of the three PAHs studied. For the NH annual average, uncertainty in $K_{BC-Water}$ contributes 63% of the total uncertainty, with k_{OH} uncertainty contributing 30%, and the uncertainty in ΔH_{vap} , European, and North American emissions making up the other 7%. This behavior changes little between the winter and summer season.

In the Arctic, $K_{BC-Water}$ is the leading source of parametric uncertainty for BaP. It contributes 55% annually, while k_{OH} contributes 35% and 6% is due to ΔH_{vap} . During the relatively photochemistry-free winter months, the contribution from k_{OH} drops to 3%, and the difference is made up by increases in the contributions of ΔH_{vap} (to 11%), and European emissions (to 29%). In the summer, the opposite occurs and k_{OH} uncertainty contributes 52% of the total.

Across all three PAHs, the contribution of physicochemical parameter uncertainty makes up more than 94% of the NH average parametric uncertainty. This is because a large fraction of the globe is far from emission sources, so wide spatial average concentrations are more sensitive to the uncertainty in the atmospheric lifetime than

they are to emissions magnitude. In the case of PYR, parametric uncertainty in the atmospheric lifetime is almost entirely due to uncertainty in the oxidation rate because of the extremely high uncertainty in oxidation rate constant. For PHE, k_{OH} also contributes most to uncertainty because PHE is mostly found in the gas phase. In the case of BaP, the uncertainty in the atmospheric lifetime is due to both the highly uncertain gas phase oxidation rate, but also the amount of BaP found in the particulate phase, which is primarily controlled by BC partitioning. Because of its nature as a mostly particulate matter-bound PAH, BaP uncertainty has a larger contribution from the uncertainty in $K_{BC-Water}$ and ΔH_{vap} , which together control partitioning to BC.

Closest to each emissions source region, uncertainty in that region's emissions becomes most important, as removal during transport has not had time to take effect. Europe is the region with sources closest to the Arctic, and therefore European emissions uncertainty contributes more to simulated Arctic concentration uncertainty than other regional emissions. The emissions uncertainty contribution reaches a maximum during the winter, when concentrations of all three PAHs are highest due to lower loss rates, making it an important factor in the quantification of PAH transport to the Arctic.

2.4.3 Observation-constrained parameter distributions

We constrain the probability distributions of parameter values using the spatially distributed modeled and observed concentrations as described in the Methods section. Figure 2-2 shows the observation-derived likelihood distributions, and prior and posterior probability distributions of the two most important parameters for model uncertainty at the measurement sites. PHE's and PYR's leading parameters are constrained by the analysis, while BaP's are effectively unconstrained.

As shown in Figure 2-2(a), for PHE, the highest observation-constrained likelihood comes when k_{OH} is highest and the European regional emission rate is low. The result is that the posterior distributions for k_{OH} and E_{Europe} have maxima at higher and lower values, respectively. Figure 2-2(b) shows a similar constraining effect of the

observations for PYR’s k_{OH} , which is shifted higher, while the EEurope posterior distribution is narrowed around the same value as the prior distribution. Figure 2-2(c) shows that the measurement comparison added no constraints to the prior parameter distributions for BaP (neither confirming nor denying the assumed prior), due to the larger uncertainties in both its simulated and observed concentrations.

After constraint by the measurement data, we estimate new most likely values for PYR’s and PHE’s k_{OH} and rate of emission in Europe. The a priori best estimate of k_{OH} for PYR was $7 \times 10^{-11} \text{ cm}^{-3} \text{ s}^{-1}$, while the updated best estimate is $1 \times 10^{-10} \text{ cm}^{-3} \text{ s}^{-1}$. The prior estimate of k_{OH} for PHE of $1.9 \times 10^{-11} \text{ cm}^{-3} \text{ s}^{-1}$ is updated to $2.3 \times 10^{-11} \text{ cm}^{-3} \text{ s}^{-1}$. We lower our best estimates of European emissions for PHE from 5.8 kt/yr to 4.1 kt/yr.

2.5 Discussion

Through the uncertainty attribution described above, we identify the key parameters for which reducing uncertainty would improve our ability to model long-range transport of PAHs. For PHE and PYR, k_{OH} uncertainty has the largest impact on model results, while for BaP k_{OH} , $K_{BC-Water}$, and ΔH_{vap} all contribute to uncertainty in simulated concentrations. These results are similar to findings for multimedia models of other environmental toxics, which indicate that degradation rates and partition coefficients are the largest contributors to parametric uncertainty [47, 44]. Across all three PAHs, more precise experimental quantification of k_{OH} could greatly reduce parametric model uncertainty. In particular for PYR and BaP, the lack of experimental values of k_{OH} leads to an additional step in the propagation of uncertainty, as the value of k_{OH} used in the model is itself a parametrization. With reduced k_{OH} uncertainty, we would be better able to constrain PAH emissions using observations of concentrations, and we would improve our ability to use modeling to inform policy [29].

Close to sources, emissions uncertainty gains importance, and reductions in emissions uncertainties should target the leading contributors to those uncertainties. PAH

emissions processes with the largest uncertainties in emissions factors include the use of traffic gasoline, diesel, and kerosene, industrial coal burning, and non-transport petroleum combustion. Precise quantification of these emissions factors would greatly reduce emissions uncertainty, especially in the North American and European regions. Some of the uncertainty involved, however, is unsolvable in current set-up of emissions inventories, since a single emission factor applies to all e.g. traffic gasoline use, despite PAH emissions from gasoline use depend on combustion temperatures, type of engine, type of exhaust system, etc. Such uncertainties would require a much more detailed type of emissions inventory that would be impractical to apply globally.

We are able to quantitatively attribute simulated concentration uncertainty to individual model parameters while accounting for non-linear model responses in a computationally efficient manner. Because of the method’s relatively low number of required model runs, it could be applied to other spatially resolved environmental models for low-cost but detailed identification of leading contributors to parametric uncertainty. The detailed parametric uncertainty analysis that this method provides is an important aspect of environmental transport model simulations that is commonly unreported in the literature. This type of analysis should be carried out for other substances and models, as the conclusions from our simulations of PAHs specifically may not apply to other substances or models. This is evident in comparison to the first-order uncertainty analysis for BETR Research PCB153 simulations [69], which suggests that emissions uncertainties account for more than 90% of the simulated atmospheric concentration parametric uncertainty under current climate and emissions.

We constrain physicochemical and emissions parameters using measurements, with updated uncertainty distributions for k_{OH} and E_{Europe} for PHE and PYR. While this method represents a quantitative improvement over traditional model sensitivity tests, in which parameters are altered based on forward matches to observations, our approach also has important limitations. The constraint relies on the comparison of concentrations measured at a point to the average concentration within a GEOS-Chem grid-box. While we account for this through an estimate of represen-

tativeness error, spatial heterogeneities within the grid-box are not represented and could introduce an unquantified bias in the comparisons due to this mismatch of spatial resolutions. We do not optimize for the spatial distribution of emissions in this study, which precludes the ability to account for a local emission source that could be driving observed concentrations at a site. Our analysis also relies on the quantification of the emissions parameters and their uncertainty at the inventory’s national level, and any potential biases in these estimates would propagate to our results. For example, an underestimation of the uncertainty in biomass burning emissions factors in the inventory would propagate through the model to result in an underestimate of concentration uncertainty.

While we quantify the impact of uncertainties in regional emission magnitudes and physicochemical properties on simulated concentrations in detail, there are other sources of uncertainty in simulated concentrations. Emissions can vary substantially temporally, and on spatial scales finer than those considered here. These temporal and spatial resolution mismatches between the simulations and reality will have a more limited effect on large spatial and time averages than on shorter-term localized concentrations. Along with direct emissions, secondary emissions (revolatilization) from surface media can affect atmospheric PAH concentrations, and these secondary sources are not resolved in this work. The accuracy and time-resolution of prescribed concentrations of particulate matter and OH used in the model can also introduce uncertainty, but this uncertainty is significantly smaller than that due to their associated chemical parameters [21]. There is also non-parametric uncertainty associated with the particle partitioning scheme used, as deviations from measurements can be large, especially for smaller PAHs [36] whose concentrations have lower sensitivity to particle partitioning. Theoretical issues have been identified with the parametrization of partition coefficients [23], which we have not accounted for here. Limitations of particle partitioning schemes for PAHs in GEOS-Chem have been investigated in detail previously [20]. Considering these uncertainties, our results suggest that for BaP, further constraints on partitioning properties would improve our ability to capture long-range transport.

Chemical transport modeling is susceptible to a variety of sources of uncertainty that are not unique to the simulation of PAHs. Advection in the atmosphere is carried out on a large scale that is only representative of the actual advection in the atmosphere on a coarse scale. This advection is based on meteorological reanalysis fields that have their own uncertainty. Prescribed precipitation also contributes to uncertainty in wet deposition. However, many of these processes in GEOS-Chem are evaluated and constrained using simulations of other atmospheric constituents (e.g. carbon monoxide, ozone) for which measurement data are less uncertain and more widely available [35, 70, 52]. The source of uncertainty most difficult to quantify is that which is associated with PAH-specific processes not represented by the model (e.g. on-particle oxidation reactions other than ozonation). A process that is not described by the model would not be represented in a parametric uncertainty analysis, and depending on the importance of the process could be a major source of unquantified uncertainty.

Based on model sensitivity, the most effective locations for hypothetical future measurement sites that could be used to improve the constraint of the most important PAH physicochemical properties are far from sources and are generally in regions where wet deposition is relatively less important, particularly in the Southern Hemisphere. These locations, however, have very low PAH concentrations, below common quantification limits. The resulting measurement constraint paradox is that the locations that would best constrain physicochemical properties have concentrations that are the most difficult to measure. This means that greatly reducing model parametric uncertainty by observational constraint will require very low detection limits at long-term remote sites. Measuring these low concentrations is potentially achievable for the gas phase using passive air samplers, which accumulate greater contaminant mass over longer periods of time than traditional active samplers [29].

The results we present give important insight into the parametric uncertainty distributions of simulated PAH concentrations and their relationship to specific inputs. Our analysis demonstrates that there is a need to reduce the large parametric uncertainties stemming from physicochemical property data for PAHs, and identifies the

Parameter	Role	BaP Value (std.)	PYR Value (std.)	PHE Value (std.)
$\log_{10} K_{BC-Water}$ (unitless)	BC partition coefficient	8.8 (0.4)	7.5 (0.2)	6.85 (0.3)
$\log_{10} K_{OA}$ (unitless)	OC partition coefficient	11.27 (0.21)	8.78 (0.08)	7.58 (0.06)
ΔH_{vap} (kJ/mol)	Enthalpy of vaporization	99.9 (7.4)	82.3 (3.9)	68.3 (8.9)
$\log_{10} K_{AW}$ (unitless)	Air-water partition coefficient	-4.42 (0.08)	-3.34 (0.07)	-2.81 (0.06)
ΔH_{sol} (kJ/mol)	Enthalpy of solvation	37.9 (17.7)	37.9 (8.9)	34.5 (2.0)
k_{OH} ($\text{cm}^3 \text{molec}^{-1} \text{s}^{-1}$) ($\log_{10} k_{OH}$ for BaP and PYR)	Gas-phase oxidation rate constant	-9.88 (0.26) ($\log_{10} k_{OH}$)	-10.1 (0.35) ($\log_{10} k_{OH}$)	1.9×10^{-11} (0.4×10^{-11})
k_{O_3} (10^{-7}s^{-1} , at 50ppb O_3)	On-particle oxidation rate constant	24.5 (3.5)	2.92 (1.21)	2.91 (0.92)

Table 2.1: Uncertainty of physicochemical properties in GEOS-Chem PAH simulations (means and standard deviations of normal distributions)

properties which contribute most to model parametric uncertainty. While our analysis shows that long-term measurement sites can be used to constrain physicochemical property values for PHE and PYR, highlighting the importance of such measurements of atmospheric PAHs, better experimental quantification of PAH properties would provide the greatest reductions in simulated concentration uncertainty. We identify quantitatively which physicochemical properties of PHE, PYR and BaP could be targeted experimentally to greatly reduce simulated concentration uncertainty.

2.6 Selected Supporting Information

The full supporting information includes physicochemical property data and associated uncertainties, emissions uncertainty information, measurement site info, data, and errors, seasonal parametric uncertainty comparisons, and parametric uncertainty contributions as a function of latitude and longitude. This information is available free of charge via the Internet at <http://pubs.acs.org/> and a subset is included below.

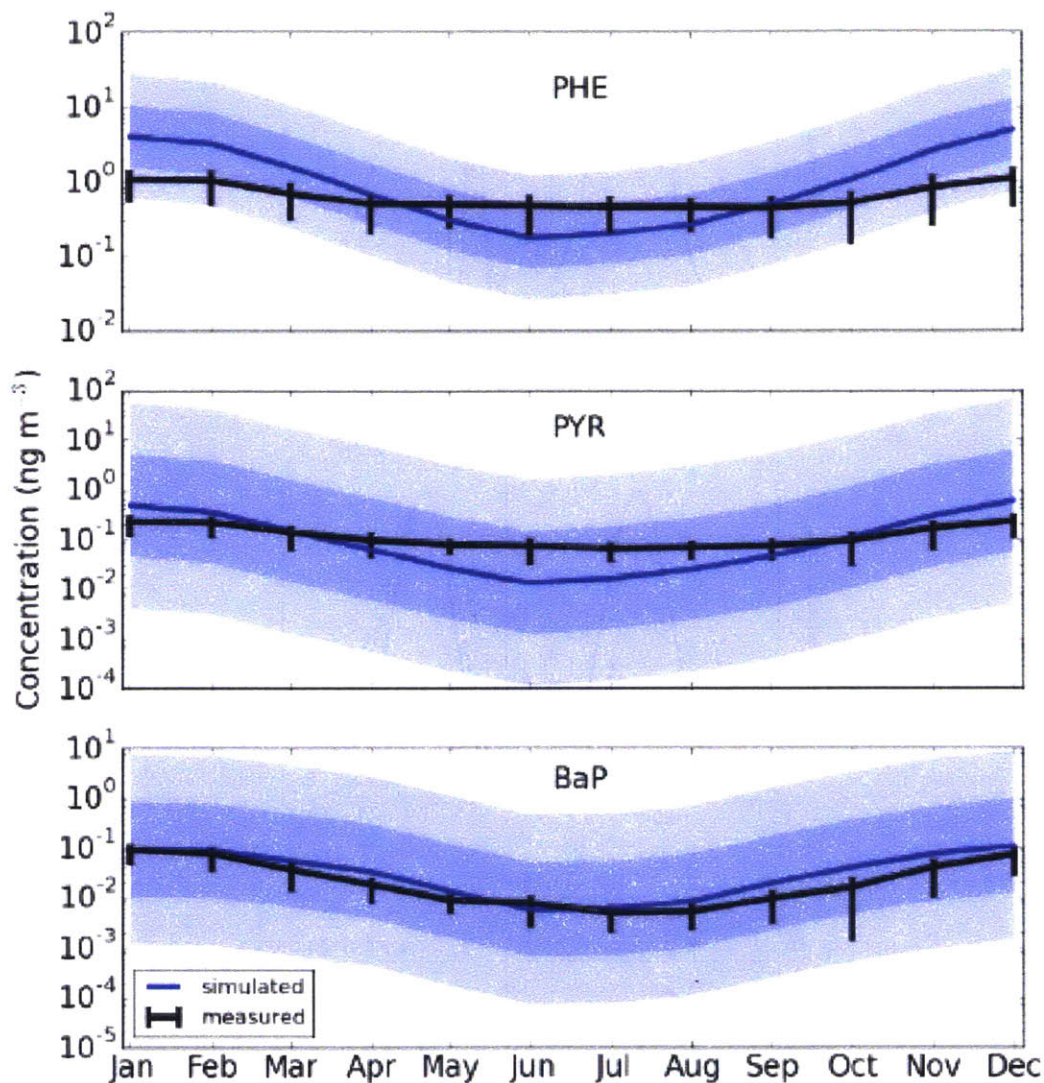


Figure 2-1: Measured and simulated total (gas and particulate) concentrations at non-urban sites for PHE (top), PYR (middle), and BaP (bottom). The black lines are means across the measurements at all non-urban sites, and their error bars show the standard deviation of the mean for each month. The blue lines are the simulated means across the same sites, with the shaded regions marking the σ and 2σ intervals of the parametric uncertainty distributions for each month.

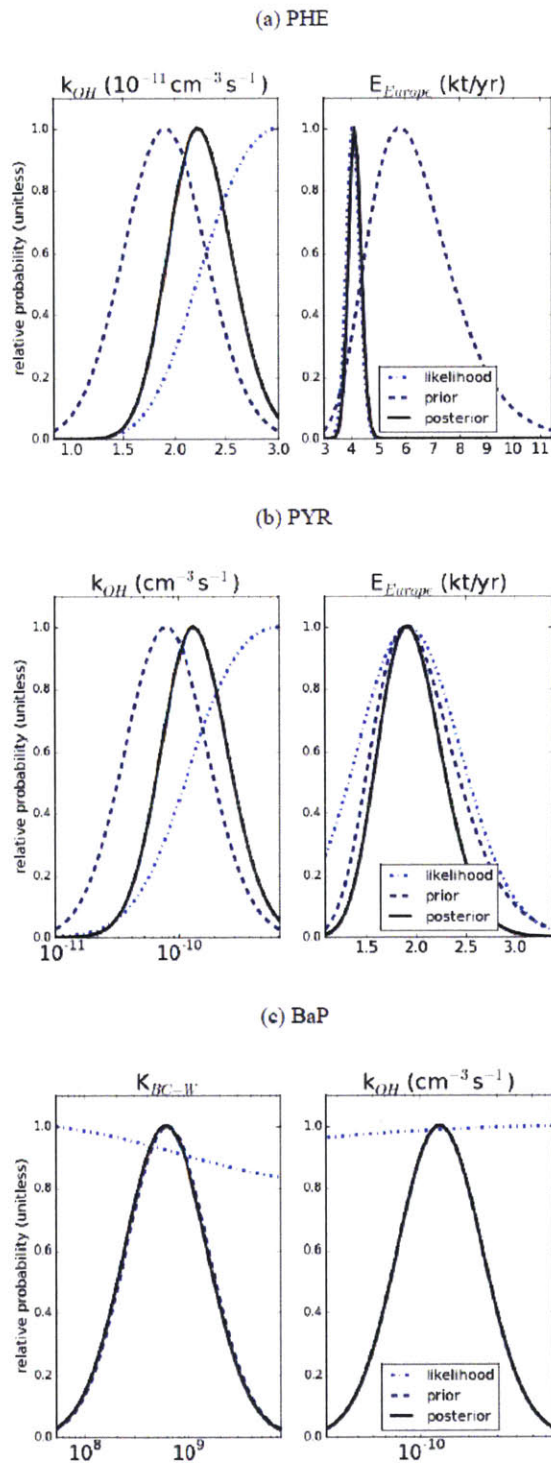


Figure 2-2: Constraint of parameter uncertainty distributions by measurement data. (a) PHE, (b) PYR, (c) BaP distributions for the two most important parameters each. Prior distributions (dashed lines), observation-based likelihoods (dot-dashed lines), and posterior distributions (solid lines) shown

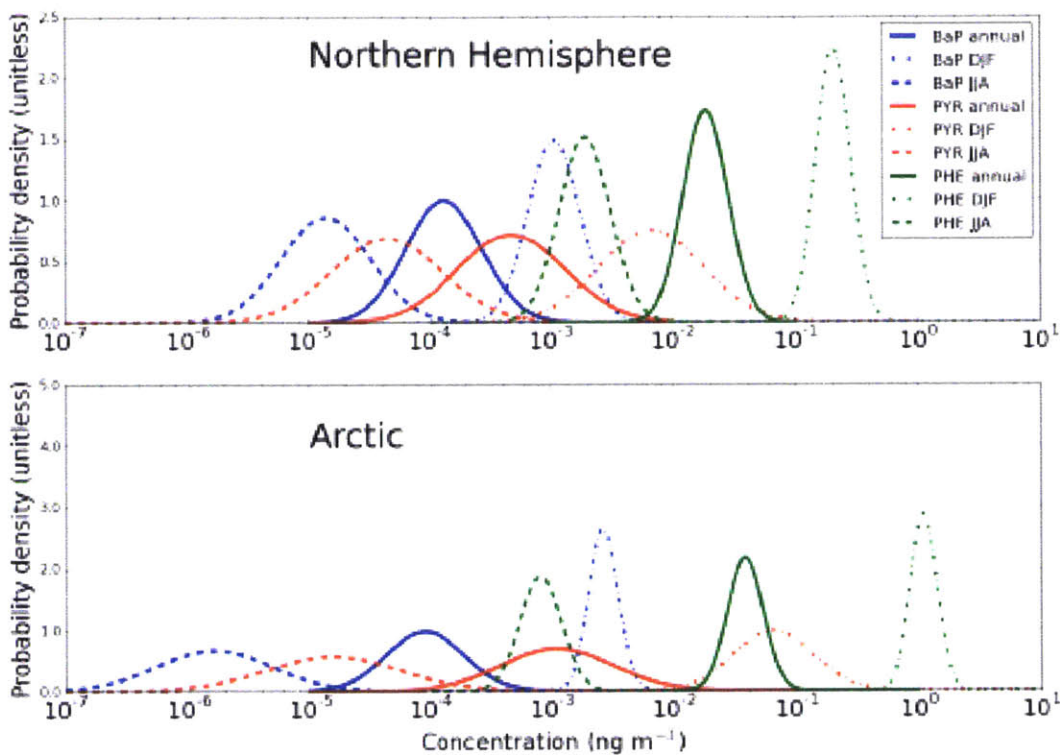


Figure 2-3: Total surface atmospheric concentration uncertainty distributions for BaP (blue), PYR (red), and PHE (green). Annual average (solid lines), winter average (dot-dashed lines), and summer average (dotted lines) shown for both Northern Hemispheric (top) and Arctic (bottom) spatial averages.

Physicochemical parameter	Literature Values	Source	Best estimate	Uncertainty
$\log K_{AW}$ (unitless)	-2.76 -2.87	1	-2.81	0.06
$\log K_{BC-w}$ (unitless)	6.6 7.1	2	6.85	0.3
$\log K_{OA}$ (unitless)	7.64 7.52	1	7.58	0.06
ΔH_{vap} (kJ/mol)	52.97 55.60 59.35 55.70 69.58 67.98 74.26 80.62 68.58 71.88 73.88 76.38 73.18 76.38	3	68.3	8.9
ΔH_{sol} (kJ/mol)	32.5 36.3 34.8	5	34.5	2.0
k_{OH} ($\text{cm}^3 \text{ molec}^{-1} \text{ s}^{-1}$)	27×10^{-12} 31×10^{-12} 13×10^{-12}	4 5 6	19×10^{-12}	4×10^{-12}
k_{O_3B} (molec cm^{-3})	2.15×10^{15}	7	2.15×10^{15}	1×10^{15}

Table 2.2: Physicochemical parameter data for PHE

Physicochemical parameter	Literature Values	Source	Best estimate	Uncertainty
$\log K_{AW}$ (unitless)	-3.27 -3.41	1	-3.34	0.07
$\log K_{BC-w}$ (unitless)	7.3 7.7	8 9	7.5	0.2
$\log K_{OA}$ (unitless)	8.86 8.70	1	8.78	0.08
ΔH_{fus} (kJ/mol)	15.31	5		
ΔH_{sub} (kJ/mol)	97.5 94.10 97.5 101 80.0 100.4 91.20 94.14 103.1	5		
ΔH_{vap} (kJ/mol)		derived from ΔH_{fus} and ΔH_{sub}	82.3	3.9
ΔH_{sol} (kJ/mol)	30.5 47.7 35.4	5	37.9	8.9
Ionization Potential (eV)	7.41 7.7 7.53 7.55 7.06 8.13 7.73	10	7.6	0.3
$\log_{10} k_{OH}$ ($\text{cm}^3 \text{molec}^{-1} \text{s}^{-1}$)		11	-10.1	0.35
k_{O3B} (molec cm^{-3})	3×10^{15}	7	3×10^{15}	2×10^{15}

Table 2.3: Physicochemical parameter data for PYR

Physicochemical parameter	Literature Values	Source	Best estimate	Uncertainty
$\log K_{AW}$ (unitless)	4.51	1	-4.42	0.08
	4.34			
$\log K_{BC-w}$ (unitless)	9.2	2	8.8	0.4
	8.4			
$\log K_{OA}$ (unitless)	11.48	1	11.27	0.21
	11.06			
ΔH_{fus} (kJ/mol)	15.10	3		
ΔH_{sub} (kJ/mol)	100.0	3		
	118.4			
	118.4			
ΔH_{vap} (kJ/mol)	100.6	12	99.9	7.4
ΔH_{sol} (kJ/mol)	25.6 (value for benzo[e]pyrene)	3	37.9 (value for pyrene)	17.7 (uncertainty for pyrene doubled)
Ionization Potential (eV)	7.1	13	7.38	0.25
	7.12	14		
	7.12	15		
	7.73	16		
	7.56	17		
	7.6	18		
	7.41	19		
7.39	20			
$\log_{10} k_{OH}$ ($\text{cm}^3 \text{molec}^{-1} \text{s}^{-1}$)		11	-9.88	0.26
k_{O_3B} (molec cm^{-3})	2.8×10^{13}	7	2.8×10^{13}	0.4×10^{13}

Table 2.4: Physicochemical parameter data for BaP

Observation site	Lat.	Lon.	Source network	total BaP [ng/m ³]	total PYR [ng/m ³]	total PHE [ng/m ³]
Sleeping Bear Dunes, USA	44.76	-86.06	IADN	0.03 (0.01-0.10)	0.10 (0.03-0.29)	0.60 (0.22-1.64)
Eagle Harbor, USA	47.46	-88.15	IADN	0.011 (0.005-0.025)	0.05 (0.02-0.11)	0.40 (0.18-0.87)
Kosetice, Czech Rep.	49.58	15.08	EMEP	0.31 (0.2-0.45)	1.23 (0.89-1.70)	5.63 (4.08-7.77)
High Muffles, UK	54.33	-0.81	EMEP	0.06 (0.02-0.14)	0.44 (0.18-1.06)	5.28 (1.98-14.05)
Westerland, Germany	54.92	8.3	EMEP	0.08 (0.05-0.14)	0.53 (0.32-0.88)	2.46 (1.44-4.22)
Rao, Sweden	57.4	11.92	EMEP	0.06 (0.04-0.10)	0.25 (0.17-0.37)	1.08 (0.75-1.55)
Aspvreten, Sweden	58.8	17.38	EMEP	0.06 (0.03-0.10)	0.24 (0.15-0.39)	1.26 (0.87-1.82)
Lahemaa, Estonia	59.5	25.9	EMEP	0.13 (0.08-0.22)		
Pallas, Finland	68	24.15	EMEP	0.02 (0.01-0.03)	0.08 (0.05-0.12)	0.40 (0.27-0.58)
Spitsbergen, Norway	78.9	11.88	EMEP	0.003 (0.002-0.004)	0.019 (0.016-0.026)	0.063 (0.050-0.071)
Alert, Canada	82	-62	EC	0.002 (0.0015-0.0026)	0.025 (0.017-0.034)	0.065 (0.052-0.094)

IADN: Integrated Atmospheric Deposition Network, EMEP: European Monitoring and Evaluation Programme, EC: Environment Canada

Table 2.5: Site info, annual average total concentrations (and ± 1 standard deviation of observational error) for PAH observation sites.

(i) PHE – NH	k_{cor}	East Asian Em.	European Em.	North Amer. Em.
Annual	94%	0%	5%	1%
DJF	85%	1%	12%	2%
JJA	97%	0%	2%	1%

(ii) PHE – Arctic	k_{cor}	European Em.	North Amer. Em.
Annual	70%	29%	1%
DJF	35%	64%	1%
JJA	84%	14%	2%

(iii) PYR – NH	k_{cor}	European Em.
Annual	99%	1%
DJF	98%	2%
JJA	99%	1%

(iv) PYR – Arctic	k_{cor}	European Em.
Annual	97%	3%
DJF	94%	6%
JJA	99%	1%

(v) BaP – NH	k_{cor}	K_{BC-W}	ΔH_{vap}	East Asian Em.	European Em.	North Amer. Em.
Annual	30%	63%	5%	0%	1%	1%
DJF	30%	62%	4%	1%	2%	1%
JJA	35%	59%	4%	0%	1%	1%

(vi) BaP – Arctic	k_{cor}	K_{BC-W}	ΔH_{vap}	European Em.	North Amer. Em.
Annual	35%	55%	6%	3%	1%
DJF	3%	56%	11%	29%	1%
JJA	52%	43%	3%	1%	1%

Table 2.6: Contributions of leading physicochemical property and regional emission uncertainties to overall uncertainty in Northern Hemisphere (NH) and Arctic concentrations of PHE (i and ii), PYR (iii and iv), and BaP (v and vi). Contributions are expressed as percentages of total uncertainty accounted for by each individual parameter rounded to the nearest percentage point. Parameters contributing <1% are not included.

2.6.1 Tables 2.2 - 2.4 data sources

(1) Ma, Y.-G.; Lei, Y.; Xiao, H.; Wania, F.; Wang, W.-H. Critical review and recommended values for the physical-chemical property data of 15 polycyclic aromatic hydrocarbons at 25 °C. *J Chem Eng Data* 2010, 55, 819-825.

(2) Lohmann, R.; Lammel, G. Adsorptive and absorptive contributions to the gas-particle partitioning of polycyclic aromatic hydrocarbons: State of knowledge and recommended parametrization for modeling. *Env. Sci Technol* 2004, 38, 3793-3803.

(3) Shiu, W.-Y.; Ma, K.-C. Temperature dependence of physical-chemical properties of selected chemicals of environmental interest. I. Mononuclear and polynuclear aromatic hydrocarbons. *J Phys Chem Ref Data* 2000, 29, 41-130.

(4) Brubaker, W. W.; Hites, R. A. OH reaction kinetics of polycyclic aromatic hydrocarbons and polychlorinated dibenzo-p-dioxins and dibenzofurans. *J Phys Chem A* 1998, 102, 915-921.

(5) Atkinson, R. Kinetics and mechanisms of the gas-phase reactions of the hydroxyl radical with organic compounds. *J Phys Chem Ref Data* 1989, Monograph 1, 1-246.

(6) Kwok, E. S. C.; Harger, W. P.; Arey, J.; Atkinson, R. Reactions of Gas-Phase Phenanthrene under Simulated Atmospheric Conditions. *Environ. Sci. Technol.* 1994, 28 (3), 521-527.

(7) Kahan, T. F.; Kwamena, N.-O. A.; Donaldson, D. J. Heterogeneous ozonation kinetics of polycyclic aromatic hydrocarbons on organic films. *Atmos Env.* 2006, 40, 3448-3459.

(8) Barring, H.; Bucheli, T. D.; Broman, D.; Gustafsson, O. Soot-water distribution coefficients for polychlorinated dibenzo-p-dioxins, polychlorinated dibenzofurans and polybrominated diphenylethers determined with the soot cosolvency-column method. *Chemosphere* 2002, 49 (6), 515-523.

(9) Walters, R. W.; Luthy, R. G. Equilibrium adsorption of polycyclic aromatic hydrocarbons from water onto activated carbon. *Environ. Sci. Technol.* 1984, 18, 395-403.

- (10) Kazakov, S. M.; Kaputerko, M. N.; Suchkov, V. A. Determination of first ionization potentials from spectra of electronic energy loss in the vapor of polyatomic organic compounds. *J. Appl. Spectrosc.* 1999, 66 (3), 375-379.
- (11) Biermann, H. W.; MacLeod, H.; Atkinson, R.; Winer, A. M.; Pitts, J. N. Kinetics of the gas-phase reactions of the hydroxyl radical with naphthalene, phenanthrene, and anthracene. *Env. Sci Technol* 1985, 19, 244-248.
- (12) Odabasi, M.; Cetin, E.; Sofuoglu, A. Determination of octanol-air partition coefficients and supercooled liquid vapor pressures of PAHs as a function of temperature: Application to gas-particle partitioning in an urban atmosphere. *Atmos Env.* 2006, 40, 6615-6625.
- (13) Clar, E.; Schmidt, W. Correlations between photoelectron and UV absorption spectra of polycyclic hydrocarbons. The pyrene series. *Tetrahedron* 1979, 35, 1027.
- (14) Akiyama, I.; Li, K. C.; LeBreton, P. R.; Fu, P. P.; Harvey, R. G. Ultra-violet photoelectron studies of polycyclic aromatic hydrocarbons. The ground-state electronic structure of aryloxiranes and metabolites of benzo[a]pyrene. *J Phys Chem* 1979, 83, 2997.
- (15) Boschi, R.; Murrell, J. N.; Schmidt, W. Photoelectron spectra of polycyclic aromatic hydrocarbons. *Faraday Discuss Chem Soc* 1972, 54, 116.
- (16) Briegleb, G. Electron affinity of organic molecules. *Angew Chem Intern Ed* 1964, 3, 617.
- (17) Birks, J. B.; Stifkin, M. A. $\dot{\text{A}}$ -Electronic excitation and ionization energies of condensed ring aromatic hydrocarbons. *Nature* 1961, 191, 761.
- (18) Matsen, F. A. Electron affinities, methyl affinities, and ionization energies of condensed ring aromatic hydrocarbons. *J Chem Phys* 1956, 24, 602.
- (19) Clar, E.; Schmidt, W. Correlations between photoelectron and phosphorescence spectra of polycyclic hydrocarbons. *Tetrahedron* 1976, 32, 2563.
- (20) Dewar, M. J. S.; Goodman, D. W. Photoelectron spectra of molecules. Part 5.—Polycyclic aromatic hydrocarbons. *J Chem Soc Faraday Trans 2* 1972, 68, 1784.

Chapter 3

Uncertainty and variability in atmospheric PFCA formation

This chapter has been published for discussion and is currently under review by the journal *Atmospheric Chemistry and Physics*. (No.: acp-2016-679)

3.1 Abstract

Perfluorocarboxylic acids (PFCAs) are environmental contaminants that are highly persistent, bio-accumulative, and have been detected along with their atmospheric precursors far from emissions sources. The importance of precursor emissions as an indirect source of PFCAs to the environment is uncertain. Modeling studies have used degradation mechanisms of differing complexities to estimate the atmospheric production of PFCAs, and these differing mechanisms lead to quantitatively different yields of PFCAs under differing atmospheric conditions. We evaluate PFCA formation with the most complete degradation mechanism to date to our knowledge, using a box model analysis to simulate the atmospheric chemical fate of precursors to long-chain PFCAs.

We calculate long-chain PFCA formation theoretical maximum yields for the degradation of precursor species at a representative sample of atmospheric conditions from a three dimensional chemical transport model, and estimate uncertainties

in such calculations for urban, ocean, and Arctic conditions using polynomial chaos methods. We find that atmospheric conditions farther from pollution sources have both higher capacities to form long chain PFCAs and higher uncertainties in those capacities.

Our calculations of theoretical maximum yields indicate that under typical Northern Hemisphere conditions, less than 10% of emitted precursor may reach long-chain PFCA end products. This results in a possible upper bound of 2-50 t/yr of long-chain PFCA (depending on quantity of emitted precursor) produced in the atmosphere via degradation of fluorotelomer products. However, transport to high-yield areas could result in higher yields. While the atmosphere is a potentially growing source of long-chain PFCAs in the Arctic, oceanic transport and interactions between the atmosphere and ocean may be relatively more important pathways to the Arctic for long-chain PFCAs.

KEYWORDS: PFCA, PFAS, FTOH, perfluoroalkyl, perfluorocarboxylic acids, per- and polyfluorinated chemicals

3.2 Introduction

Perfluorocarboxylic acids (PFCAs) are environmental contaminants that are highly persistent, bio-accumulative [40, 39, 13], and have been detected along with their atmospheric precursors far from emissions sources [73, 54, 56] in snow [71], precipitation [49], and biota [27]. Of particular environmental interest are the long-chain PFCA (lcPFCA) homologues such as PFOA (8-Carbon chain), due to the increase of detrimental effects with chain length [40, 39, 13]. While lcPFCAs are not regulated internationally, reducing lcPFCA emissions has been the focus of some national policy actions due to their detrimental health effects [60], and as a result, direct emissions have been decreasing globally. At the same time, emissions of atmospheric precursors of PFCAs are rising [64], leading to an increasing indirect source of PFCAs to the environment. These precursors, including fluorotelomer alcohols (FTOHs), react with atmospheric photochemical species [15] in a multi-stage process to form PFCAs [75].

However, the importance of precursor emissions as an indirect source of lcPFCAs to the environment is uncertain. Estimated yields of PFCAs from precursors can vary based on differences in the formation mechanism assumed, quantitative uncertainty in reaction rate constants, and ambient concentrations of other atmospheric species. Here, we use a box model analysis to quantitatively estimate potential upper-limit atmospheric yields of PFCAs, incorporating uncertainty in the precursor degradation mechanism and variability of atmospheric PFCA formation due to photochemical background conditions.

Previous studies have estimated yields of lcPFCAs from the degradation of FTOHs in the atmosphere [72, 61]. However, studies have indicated that other emitted atmospheric precursors exist in the form of other fluorotelomer compounds [75, 64, 65, 74, 9]. Rate coefficients for the reactions in the PFCA formation mechanism are uncertain, affecting estimated yields. The atmospheric formation of PFCAs depends on reactions of fluorinated intermediates [68, 12] with commonly studied photochemical species, such as HO_x and NO_x species, as well as ultraviolet light. These species vary greatly over different environments in the atmosphere, affecting the quantity of lcPFCA produced.

Modeling studies have used degradation mechanisms of differing complexities to estimate the atmospheric production of PFCAs, and these differing mechanisms lead to quantitatively different yields of lcPFCAs under differing atmospheric conditions. Wallington et al. [61] simulated the atmospheric degradation of 8:2 FTOHs using the IMPACT atmospheric chemistry model, finding that PFOA yields ranged from 1-10% depending on location and time. Yarwood et al. [72] used a higher resolution atmospheric chemistry model over North America to estimate that degradation yielded approximately 6% PFOA on average, and much less than 1% PFNA. Schenker et al. [46], using a global-scale multispecies mass-balance model with simplified chemistry, found that precursor transport and degradation could contribute to perfluorocarboxylates observed in the Arctic, and that rate constant uncertainty was an important contributor to uncertainty in their results [46].

In our work, we evaluate PFCA formation with the most complete degradation

mechanism to date to our knowledge, including the reactions presented in the studies of Wallington et al. [61] and Yarwood et al. [72], and the review of Young and Mabury [75]. We use a box model analysis to simulate the atmospheric chemical fate of fluorotelomer aldehyde (FTAL), a common early product in the degradation of many of the different precursor species, including FTOHs. We quantitatively estimate the influence of uncertainty in rate coefficients for calculations of PFCA yields using polynomial chaos methods, which have been used previously in the context of chemical reaction mechanisms [43] and atmospheric chemistry modeling in particular [11, 58]. We further examine the influence of different atmospheric chemical conditions on upper-limit PFCA formation based on output from a three-dimensional chemical transport model. We conclude by estimating potential upper limits for atmospherically formed PFCAs from emitted precursors, and compare our yield results to observed atmospherically formed PFCAs.

3.3 Methods

We use a box model representation of the chemical reactions that lead to atmospheric PFCA formation to calculate yields per unit precursor species. We calculate yields of PFOA (8 Carbons) and PFNA (9 Carbons) from the degradation of 8:2 fluorotelomer precursors. We use prescribed concentrations of photochemical species from data sources described below. To quantify an upper limit of possible atmospheric PFCA formation, we calculate yields of PFOA and PFNA in the absence of non-chemical loss processes. Thus, our calculations represent an upper limit of the PFCA formation capacity of the atmosphere at given photochemical conditions.

3.3.1 Mechanism and Box Model

In our box model, we use a precursor degradation mechanism which builds on the work of previous modeling efforts [61, 72] and includes reactions from recent literature [75]. The chemical reactions included are listed in Appendix A. The mechanism defines the degradation of fluorotelomer aldehyde, which we use as a generic precursor as it

is the first degradation product of many emitted volatile fluorotelomer compounds such as FTOHs and FT-iodides. Since this generic precursor is the common product among the reactants that precede it, its use as a starting point will not affect yield calculations. This FT-aldehyde can be oxidized by OH or photolyzed to form peroxy or acylperoxy radicals. These radicals, in turn, react with NO, NO₂, RO₂, and HO₂ to form stable intermediates. These stable intermediates can again be radicalized by further reaction with OH and ultraviolet light, with more analogous radical reactions leading to either stable PFCAs or shorter chain intermediates. Reaction products which have chain lengths shorter than PFOA are neglected in our calculations. The degradation chemistry is depicted in Figure 3-1, with each line representing a different reaction and each node representing a different intermediate species or end product.

We use a box model of the PFCA formation chemistry to calculate yields of PFOA and PFNA from precursor species. The single-box model simulates the chemical reactions discussed above, treating the concentrations of HO_x, NO_x, Cl, and RO₂ as constant and neglecting non-chemical loss processes such as wet and dry deposition. Simulations begin with a unit of precursor species and are carried out until all of the initial precursor has reached one of the reaction end-points (PFNA, PFOA, or shorter-chain PFCAs). The yield of each end species is defined as the fraction of the initial precursor that forms that species.

3.3.2 Variability of PFCA formation

To quantify the variability of PFCA formation capacity due to variations in the atmospheric chemical background of the Northern Hemisphere, we use photochemical species concentration output from the chemical transport model GEOS-Chem [4]. We use concentrations of OH, HO₂, NO, NO₂, and temperature output from a GEOS-Chem version 9.01.02 full chemistry simulation of the years 2006 and 2007 after a one year spin up.

We calculate RO₂ concentrations based on concentrations of methane, ethane, and propane from the GEOS-Chem simulation and a pseudo-steady state approximation:

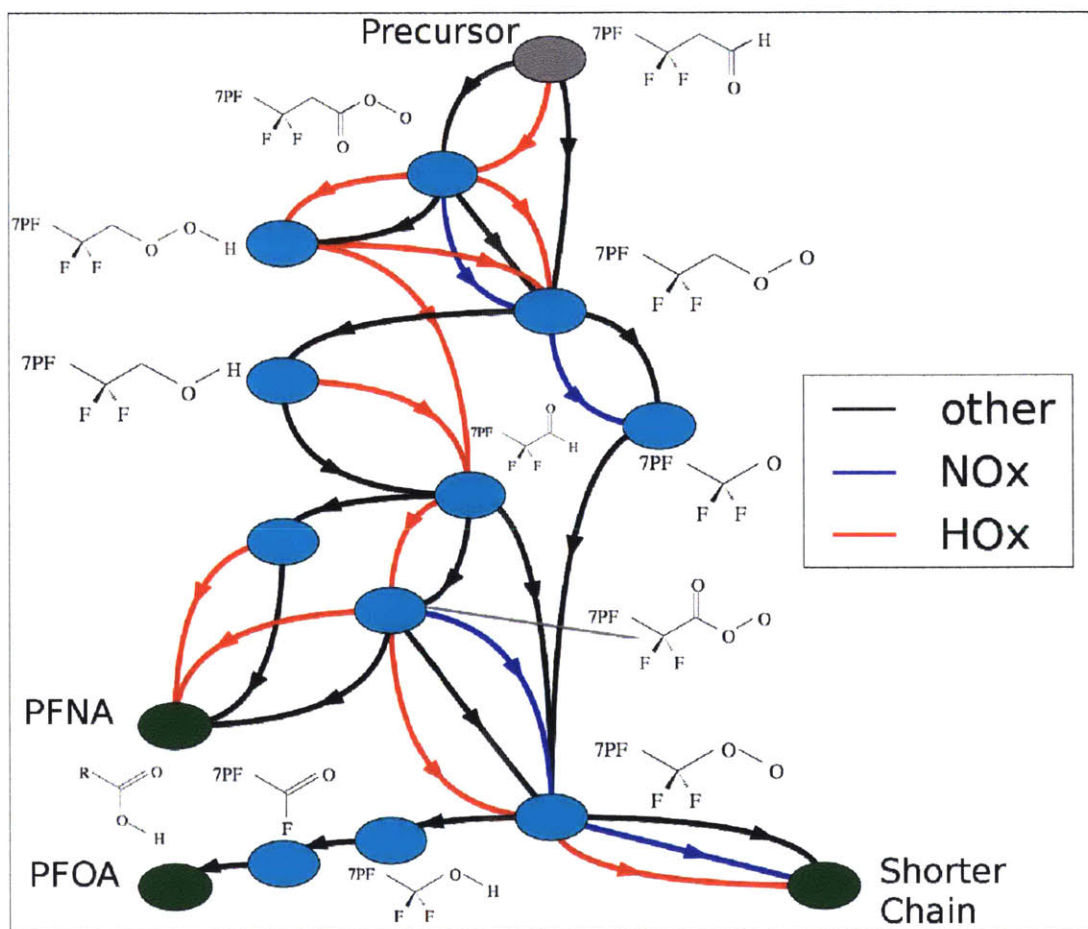


Figure 3-1: Each line represents a different reaction and each node represents a different intermediate species or end product. Reactions are color coded by the non-fluorinated reactant involved.

$$[RO_2] \approx \frac{[CH_4][OH]k_{CH_4+OH} + [C_2H_6][OH]k_{C_2H_6+OH} + [C_3H_8][OH]k_{C_3H_8+OH}}{[NO]k_{NO+RO_2} + [HO_2]k_{HO_2+RO_2}} \quad (3.1)$$

Available photons for photolysis reactions were calculated as a function of latitude and time of year based on an assumption of clear sky conditions [45], and a peak actinic flux of 1×10^{15} photons $\text{cm}^{-2} \text{s}^{-1}$ at 90 degrees solar zenith angle [51]. We use daily GEOS-Chem output concentrations from winter (January) and summer (July) of 2007 as a representative sample of the variability of atmospheric conditions in the Northern Hemisphere.

For the photochemical conditions corresponding with each surface grid box and time of the GEOS-Chem output, we perform a box model run to calculate yields and formation times of PFOA and PFNA. This results in 1656 chemical environments for each of the summer and winter conditions.

3.3.3 Uncertainty Propagation

We calculate the uncertainty in yields and formation times for PFCA formation in three case environments. We use conditions chosen from the above GEOS-Chem output data set representing three distinct photochemical environments as representative test cases. We have selected one each of urban, Arctic, and ocean environments for their distinctive PFCA formation behaviors. The photochemical concentrations of each environment are detailed in Table 3.2. The urban environment is located over urban China, and is characterized by high NO_x concentrations. The ocean environment, in contrast, is located over the equatorial Pacific Ocean and is characterized by very low NO_x concentrations. The environment illustrative of Arctic PFCA formation is located over Greenland, and is much colder and has a moderate level of NO_x .

We use polynomial chaos (PC) methods to propagate uncertainty from rate constants to yields calculated by the box model. PC methods create a polynomial expansion representation of the model to propagate uncertainty in inputs to the outputs at low computational cost while being able to represent non-linear responses of out-

puts to model input parameters, as well as interactions between input parameters [58, 37, 11]. The PC-based estimator uses orthogonal polynomials to approximate GEOS-Chem model output as a function of model inputs. The polynomial expansion of the model output to be estimated takes the form

$$\eta(\zeta) = \alpha_0 + \sum_{j=1}^d \sum_{k=1}^M \alpha_{j,k} H_j(\zeta_k) + \sum_{k=1}^{M-1} \sum_{l=k+1}^M \beta_{k,l} H_1(\zeta_k) H_1(\zeta_l) + \dots + \text{Order}(d \geq O > 2) \quad (3.2)$$

where the estimator η of degree d is a function of the polynomials H_j of order j , the M variables ζ_k representing model inputs, the expansion coefficients $\alpha_{j,k}$ and $\beta_{k,l}$, and higher order coefficients. Not shown in the equation are cross terms of degree >2 , which include the product of up to d Hermite polynomials of different variables, analogous to the second order cross terms shown. In this study, we truncate the polynomial after third order. To obtain the expansion coefficients, one model run at a unique set of inputs is performed for each term in the equation [57]. The set of inputs for the model runs for each degree's terms are the values corresponding to the roots of the next degree's polynomials. The outputs of these model runs and the corresponding sets of input values are used to set up a system of equations to solve for the expansion coefficients [37]. We use the polynomial estimator to directly infer properties of the uncertainty distribution of model output (in this case theoretical maximum fractional yields of PFOA and PFNA) without relying on Monte Carlo methods, which is accomplished using the analytical forms of the mean and variance from the polynomial coefficients [37]. We also calculate the portion of the total output variance contributed by each rate constant using the expansion coefficients [37, 11]. We carry out a second-order expansion in the 40 uncertain reaction rate constants to calculate uncertainty distributions of PFOA and PFNA yields and attribute the importance of each reaction rate constant to the resulting uncertainty.

3.3.4 Environment Categorization

In order to categorize the differences in photochemical environments, we use the DBSCAN clustering algorithm [16] to find clusters in summer average OH-HO₂-NO

concentration space. These three species were chosen because they are the most common non-fluorinated reactants in the modeled chemistry, and because they led to the delineation of the observed behavior in yield-time space apparent by visual inspection (see Section 3.4.4). The DBSCAN algorithm is density-based, clustering based on the proximity of nearest neighbors in the chosen parameter space. The algorithm requires a priori values for its two parameters, ε , which roughly describes the size of the "neighborhood" around a datum, and N_ε , the number of other data that must be within that neighborhood to be considered a cluster. The clustering is relatively insensitive to choice of N_ε [16], but the number of clusters found in the data set depends on the value of ε chosen. We choose an N_ε value of 10 and the ε value (0.3) that gives the smallest number of clusters >1 for simplicity in categorization. This results in two major clusters accounting for $>85\%$ of the data, with the remaining data unclustered.

3.4 Results

We calculate the variability in PFOA and PFNA theoretical maximum yields for summer and winter Northern Hemisphere conditions, and quantify the uncertainty in these theoretical yields for three representative test cases. We also investigate the distinct chemical regimes in the formation of PFNA in different regions of the atmosphere under average summer conditions.

3.4.1 Variability in yields due to photochemical environment

Figure 3-2 shows histograms of theoretical maximum yields of PFOA and PFNA for each of the photochemical environments from GEOS-Chem output. Each count in the histogram corresponds to a calculation of yields carried out at the conditions from a single day and Northern Hemisphere grid-box (latitude-longitude location) from the GEOS-Chem output. For PFOA during the summer, the majority of photochemical environments result in yields of between 1% and 10%, with approximately a quarter of the environments yielding $<1\%$ and a third of environments yielding between 10%

and 30%. During the winter, the peak of PFOA yields remains between 1-10% but many more environments yield <1% and fewer yield >10% compared to during the summer.

PFNA, on the other hand, sees a peak less than 1% during the summer, but shows a third of its environments between 1% and 10%, with a small fraction of environments leading to yields higher than 80%. During the winter, PFNA formation skews toward very low yields of <0.1%. The long tails of PFNA formation environments are discussed further in Section 3.4.4.

3.4.2 Uncertainty in yields due to rate constant uncertainty

Figure 3-3 shows uncertainty in PFOA and PFNA yields due to uncertainty in the rate constants in the degradation mechanism. For both species, yields are negligible under the high-NO_x urban conditions. Under oceanic conditions far from NO_x sources, the PFOA yield is approximately 20%, with an uncertainty range of approximately 3%, and the PFNA yield is more than 80%, with an uncertainty range of approximately 5%. Under Arctic conditions, PFOA yield uncertainty ranges between 18% and 22%, and PFNA shows a distribution ranging from 17% to 20%. For both species, and especially PFNA, the range of yields due to differing photochemical conditions is much larger than the range of yields due to uncertainty at any given conditions.

3.4.3 Rate coefficient contributions to yield uncertainty

Fractional contributions of individual reactions' rate coefficient uncertainties to the resulting yield uncertainty for PFOA and PFNA formation are summarized in Table 3.3. Most reactions in the mechanism contribute to uncertainty similarly for PFOA yield under urban conditions, with reaction 16 having the largest contribution. The rate of this reaction between poly-fluorinated peroxy radicals and RO₂ radicals to form a poly-fluorinated alcohol is one of the main factors determining whether the yielded product is PFNA or a shorter chain PFCA (including PFOA), which makes it important for the uncertainties in yields for both of those end products. For ocean

conditions, reaction rate constants 15, 16, 36 and 37 dominate the contributions to PFOA yield uncertainty. Arctic conditions show reaction 37's rate constant uncertainty also playing a large role, but reaction 34 also makes a substantial contribution. Reactions 15 and 16 represent a branching in the degradation chemistry where fluorinated peroxy radicals can either branch toward PFNA formation or PFOA and shorter chain PFCAs. Likewise, reactions 34, 36, and 37 are at a branching point where shorter peroxy radicals can either react to form PFOA or even shorter chain PFCAs.

PFNA yield uncertainties are dominated by a different subset of the reaction mechanism for the Arctic environment, and see a contribution from a large number of reaction rates for the urban and ocean cases, led by reactions 16 and 2 (reaction of OH with the initial precursor), respectively. In the Arctic, reaction rate constant 16 uncertainty dominates, with reaction 14 (another peroxy radical reaction) also contributing significantly. In summary, rate constants of reactions of NO and RO₂ with poly- and per-fluorinated peroxy radicals are the dominant sources of theoretical maximum yield uncertainties for PFOA and PFNA.

3.4.4 Regime behavior in PFNA yields and formation times

Figure 3-4 shows calculated PFNA yield for each GEOS-Chem grid box and associated time of formation for summer conditions, with DBSCAN algorithm clusters in the OH-HO₂-NO space of the sample of summer atmospheric photochemical conditions. Two distinct regimes appear in the plotted space, one in which yield is low across formation times, and one in which longer formation times are associated with higher yields. As figure 3-4 shows, the clusters in OH-HO₂-NO space correspond to regimes of formation for PFNA, and to spatial regions of the atmosphere. Each of the two clusters respectively compose the majority of each of the two regimes in PFNA yield - time of formation space. Figure 3-4(b) shows that the same clusters also correspond to Arctic and lower-latitude environments, respectively. Within the lower-latitude mode, PFNA yield increases with decreasing NO concentrations, with the lowest yields occurring over land in more polluted areas and the highest yields occurring

over the oceans far from NO_x sources.

3.5 Discussion

We find a wide variety of theoretical maximum yields for both PFOA and PFNA across the Northern Hemisphere's photochemical environments. With many regions yielding less than 1% of each due to the presence of large enough quantities of NO_x , but PFOA yields of up to 40% and PFNA yields of up to 80% in some areas, the specific photochemical environment has a strong effect on the capacity of the atmosphere to yield lcPFCAs from the degradation of emitted precursors. We find that the uncertainty in these theoretical maximum yields depends on the environment as well, but is at most on the order of a few percent, much smaller than the variability caused by the diversity in photochemical environments.

We find two distinct regimes of PFNA formation capacity in the atmospheric environment, which correspond to photochemical environments found in the Arctic and at lower latitudes, respectively. The former shows relatively constant theoretical maximum yields across different conditions within the Arctic, with a large range of formation times that are independent of the yields. The second regime, on the other hand, shows that at lower latitudes there is a large range of both yields and formation times, and that longer formation times are associated with higher theoretical maximum yields. Within this regime, the higher the concentration of NO , the shorter the formation time and the lower the yield capacity. Figure 3-5 illustrates this behavior, showing the flux through different reactions in the chemical mechanism over the course of a box model run at the conditions of the three representative environments introduced in Section 3.3.3. The nodes in the diagram represent intermediate or end-product species in fluorotelomer degradation, while the lines represent the reaction fluxes, with the thickness of the lines proportional to the flux. Figure 3-5(a) and (b) show that at lower latitudes the amount of NO present strongly drives fluxes towards either short chain PFCAs (Urban, high- NO conditions) or long chain PFCAs (Ocean, low- NO conditions). The reactions of peroxy radicals with NO are too fast in the

presence of substantial NO_x to allow branching toward PFNA or PFOA formation.

The highest theoretical maximum yields and longest formation times are associated with conditions over the oceans far from sources and far from common photochemical pollution sources. Emissions of lcPFCA precursors into polluted air masses reduces the potential for those precursors to form lcPFCAs. Put another way, emissions of precursors in otherwise less-polluted regions are conducive to more lcPFCA formation per precursor emitted.

The calculations that we present are of lcPFCA theoretical maximum yields, and are the upper limits of PFOA and PFNA formation for given atmospheric conditions. In the atmosphere, non-chemical loss processes that we neglect in our model limit actual lcPFCA yields compared to their theoretical maxima. In the case of PFNA, as the areas with highest theoretical maximum yields are associated with the longest formation times, they will see larger discrepancies between theoretical and actual yields than areas with lower theoretical maximum yields. Although regions far from NO_x sources have the greatest capacity for PFNA formation, they also are most vulnerable to having concentrations of degradation intermediates reduced by wet deposition and scavenging before the degradation has reached an end product (e.g. over the equatorial oceans). We also use a generic precursor (perfluorinated aldehyde) in our calculations, which is the common first degradation product of most of the mass fraction of the fluorotelomer precursors emitted by current estimates [64]. Some fluorotelomer precursors, however, such as fluorotelomer olefins, have initial degradation products which are intermediates in the discussed degradation mechanism. If the fraction of emitted fluorotelomer products which are FT-olefins is large, this could quantitatively affect our results.

We calculate the theoretical maximum yields of lcPFCAs from precursor degradation under many atmospheric conditions, but the degradation mechanism is indicative of daytime chemistry. In the Arctic during the summer this is not problematic, but in the winter it neglects the possibility of significant nighttime chemistry involving species such as N_2O_5 and H_2O_2 that to our knowledge has not been studied. Future research could put theoretical or experimental constraints on the possible importance

of these reactions.

With respect to theoretical maximum yields in different seasons, winter conditions lead to lower yields of both PFNA and PFOA, sometimes by orders of magnitude. Young et al. [73] report a similar seasonal dependence from the Devon Ice Cap, with summer concentrations of PFOA and PFNA being an order of magnitude higher than winter concentrations in the accumulated snow profiles. For the years 2004 and 2005, the average winter PFNA concentration in those snow measurements is 18 times smaller than the average summer concentration, and for PFOA the winter average is 7 times smaller. In our calculations, those same ratios over the Canadian Arctic are 18 and 10, respectively. As the long-chain PFCA deposited on the Devon Ice Cap is most likely atmospherically generated [73, 24], this suggests consistency between our calculations of PFNA and PFOA theoretical yields and observational evidence of lcPFCA yielded through formation in the atmosphere.

The importance of the photochemical environment to lcPFCA formation, particularly the importance of the presence of NO_x , means that future air pollution reductions or increases could impact atmospheric lcPFCA yields. For instance, large reductions in NO_x emissions would lead to more lcPFCA products. However, given our results, we find that NO_x concentration reductions would have to be on the order of magnitude scale to affect theoretical maximum yields significantly.

We estimate uncertainty ranges in theoretical maximum yields for PFOA and PFNA under the ocean case conditions to be 17-22% and 78-85%, respectively, with most of the uncertainty for PFOA stemming from uncertainty in rate constants at a branching point in the degradation mechanism. In the Arctic case conditions, PFOA maximum yield has a similar value and level of uncertainty as for ocean conditions, while PFNA yields have a much lower value and slightly lower level of uncertainty. Again, under these conditions, the majority of the uncertainty is due to uncertainty in two peroxy radical reaction rate constants at branching points in the mechanism. Better understanding the quantitative relationship between rate constants at these branching points will have the greatest effect on reducing the uncertainty in theoretical maximum yields.

We quantify the uncertainty in theoretical maximum yields, which depend exclusively on the rate constants. In the atmosphere, where deposition can play an important role in lcPFCA formation, many other sources of uncertainty for yields will arise, such as rates of deposition, frequency of rainout and washout events, solubility and aqueous chemistry of intermediate species, among others. While the uncertainty due to rate constants is quantifiable based on the chemistry used in our calculations, any missing reactions in the degradation chemistry will be unquantifiable. If our mechanism is incomplete due to currently unidentified reactions, our estimates of uncertainty would underestimate the full uncertainty of the chemistry. Our estimates of the variability of lcPFCA theoretical maximum yields in the atmosphere are also uncertain due to uncertainty in the photochemical conditions used, which are output from the GEOS-Chem model. These uncertainties would be minor in this application, as the photochemical concentrations vary over orders of magnitude, while their relative uncertainties are much smaller than these variations. The uncertainty in GEOS-Chem calculations of photochemical environment is not quantified here, nor is the uncertainty due to the model grid box size's inherent smoothing of photochemical extremes. Model grid box size is unlikely to change our results in any meaningful way since the polluted regions whose representation would suffer from this type of smoothing already produce negligible quantities of lcPFCA.

The maximum yields calculated above allow us to estimate potential upper limits on the amount of atmospherically produced long-chain PFCAs given the emitted precursor quantities. The current estimate [64] of volatile 8:2 fluorotelomer compound global releases has an upper bound of 500 t/yr for the year 2010, the only year for which such a detailed estimate is available. Given the theoretical maximum yields we have calculated, this translates to 50 t/yr of lcPFCA produced atmospherically based on median yield values from our calculations. This may be an overestimate, however, considering the spatial distribution of theoretical maximum yields. In regions that precursors are emitted (over continental North America, Europe and Asia), theoretical maximum yields are less than 1%. If the precursors and intermediates reside in this type of environment for extended periods of time, the upper limit of atmospheric

lcPFCA production could be 5 t/yr or lower. However, larger yields can result when precursors are transported to higher-yield environments. These estimates of upper limit atmospheric production scale linearly with emissions, so emissions rates lower than the upper bound estimates would lead to correspondingly lower atmospheric production maxima. Depending on how long precursor and intermediate species reside in the different atmospheric regions and the distribution of emissions, yields of lcPFCAs can vary greatly. Future calculations with a detailed chemical transport model that also accounts for both deposition processes and transport in the atmosphere would allow for a best estimate of total lcPFCA production in the atmosphere over time. While the U.S. EPA Stewardship Program strives to greatly reduce lcPFCA precursors emitted due to American manufacturers, there remains the possibility of growth of precursor production in Asia in the future, meaning that atmospheric lcPFCA formation could become increasingly important as a source globally and to the Arctic. In the future, if production does shift to shorter chain fluorotelomer products, our findings will apply to correspondingly shorter chain PFCAs formed in the atmosphere, as the chemistry studied is analogous across the homologue series.

Wallington et al. [61] estimated 0.4 t/yr of PFOA entering the Arctic due to atmospheric production via 8:2 FTOH degradation; the amount entering the Arctic is less than half of global atmospheric PFOA production. This was calculated assuming 1000 t/yr of FTOH emitted to the atmosphere, which is twice the current upper bound of total fluorotelomer emissions to air. Wania [66] estimated that the amount of atmospherically generated PFCAs deposited in the Arctic peaked in 2005 at 0.154 t/yr, and that 11-21 t/yr is transported to the Arctic via the ocean. Both of these studies estimate atmospherically generated quantities of lcPFCAs which fall reasonably beneath our calculated theoretical maxima. Our results indicate, however, that the region over the oceans is the leading atmospheric environment for lcPFCA formation, meaning that transport to the Arctic via the ocean can be importantly affected by lcPFCAs formed atmospherically at lower latitudes. A detailed coupled atmosphere-ocean model could give important insights to future studies.

3.6 Conclusions

We calculate PFOA and PFNA formation theoretical maximum yields for the degradation of precursor species at a representative sample of atmospheric conditions, and estimate uncertainties in such calculations for urban, ocean, and Arctic conditions. We find that atmospheric conditions farther from pollution sources have both higher capacities to form long chain PFCAs and higher uncertainties in those capacities. The greatest uncertainty reductions can be achieved by better quantifying rate constants at the branching points of the degradation chemistry. We find that there are distinct regimes of PFNA formation behavior in different photochemical environments, dictated by the quantities of HO_x and NO_x species, but less variability in the formation of PFOA.

While we study the daytime chemistry in detail, future studies should investigate the role of nighttime chemistry in lcPFCA formation. The role of non-chemical removal processes from the atmosphere is also an important part of atmospheric lcPFCA formation, and its environmental connection to yields of formation should be investigated.

Our calculations of theoretical maximum yields indicate that most likely less than 10% of emitted precursor can reach lcPFCA end products in the Northern Hemisphere, even ignoring non-chemical losses. This results in an upper bound of 2-50 t/yr of lcPFCA (depending on quantity of emitted precursor) produced in the atmosphere via degradation of fluorotelomer products. Only a fraction of that is destined to directly deposit in the Arctic. While the atmosphere is a potentially growing source of lcPFCA in the Arctic, oceanic transport of directly emitted lcPFCAs and atmospherically generated lcPFCAs at lower latitudes are likely more important pathways to the Arctic for lcPFCA.

Table 3.1: List of reactions.

Reaction	Rate constant expression	uncertainty	source
$\text{C8F17CH2C(O)H} + \text{hv350} \rightarrow \text{C8F17CH2OO}$	1.5×10^{-21}	7.5×10^{-22}	1
$\text{C8F17CH2C(O)H} + \text{OH} \rightarrow \text{C8F17CH2C(O)OO}$	2.0×10^{-12}	0.4×10^{-12}	1
$\text{C8F17CH2C(O)H} + \text{Cl} \rightarrow \text{C8F17CH2C(O)OO}$	1.9×10^{-11}	0.2×10^{-11}	1
$\text{C8F17CH2C(O)OO} + \text{NO2} \rightarrow \text{C8F17CH2C(O)OONO2}$	$1.1 \times 10^{-11} (298./\text{T})$	0.1×10^{-11}	3
$\text{C8F17CH2C(O)OONO2} \rightarrow \text{C8F17CH2C(O)OO}$	$2.8 \times 10^{16} \exp(\text{T}/-13580)$	0.2×10^{16}	3
$\text{C8F17CH2C(O)OO} + \text{NO} \rightarrow \text{C8F17CH2OO}$	$7 \times 10^{-12} \exp(\text{T}/340)$	0.5×10^{-12}	3
$\text{C8F17CH2C(O)OO} + \text{HO2} \rightarrow \text{C8F17CH2OO}$	$3.1 \times 10^{-13} \exp(\text{T}/1040)$	0.3×10^{-13}	3,1
$\text{C8F17CH2C(O)OO} + \text{HO2} \rightarrow \text{C8F17CH2C(O)OH}$	$1.2 \times 10^{-13} \exp(\text{T}/1040)$	0.1×10^{-13}	3,1
$\text{C8F17CH2C(O)OO} + \text{CH3O2} \rightarrow \text{C8F17CH2OO}$	$1.8 \times 10^{-12} \exp(\text{T}/500)$	3.6×10^{-13}	2
$\text{C8F17CH2C(O)OO} + \text{CH3O2} \rightarrow \text{C8F17CH2C(O)OH}$	$2.0 \times 10^{-13} \exp(\text{T}/500)$	4.0×10^{-14}	2
$\text{C8F17CH2C(O)OH} + \text{OH} \rightarrow \text{C8F17CH2OO}$	$2.02 \times 10^{-14} \exp(\text{T}/920)$	0.6×10^{-14}	2
$\text{C8F17CH2C(O)OH} + \text{OH} \rightarrow \text{C8F17C(O)H}$	$1.13 \times 10^{-14} \exp(\text{T}/920)$	0.32×10^{-14}	2
$\text{C8F17CH2OO} + \text{HO2} \rightarrow \text{C8F17CH2OOH}$	$4.1 \times 10^{-13} \exp(\text{T}/750)$	0.4×10^{-13}	3
$\text{C8F17CH2OO} + \text{NO} \rightarrow \text{C8F17CH2O}$	$2.8 \times 10^{-12} \exp(\text{T}/300)$	0.14×10^{-12}	3
$\text{C8F17CH2OO} + \text{CH3O2} \rightarrow \text{C8F17CH2O}$	$1.9 \times 10^{-14} \exp(\text{T}/390)$	0.26×10^{-14}	2
$\text{C8F17CH2OO} + \text{CH3O2} \rightarrow \text{C8F17CH2OH}$	$7.6 \times 10^{-14} \exp(\text{T}/390)$	1.06×10^{-14}	2
$\text{C8F17CH2OH} + \text{OH} \rightarrow \text{C8F17C(O)H}$	$1.02 \times 10^{-13} \exp(\text{T}/-350)$	0.1×10^{-13}	4
$\text{C8F17CH2OH} + \text{Cl} \rightarrow \text{C8F17C(O)H}$	$6.5 \times 10^{-13} \exp(\text{T}/-350)$	1.0×10^{-13}	2
$\text{C8F17CH2OOH} + \text{OH} \rightarrow \text{C8F17CH2OO}$	$4.0 \times 10^{-12} \exp(\text{T}/200)$	1.0×10^{-12}	2
$\text{C8F17CH2O} \rightarrow \text{C8F17OO}$	2.5×10^1	0.1×10^1	4
$\text{C8F17C(O)H} + \text{hv350} \rightarrow \text{C8F17OO}$	1.6×10^{-21}	0.12×10^{-21}	1
$\text{C8F17C(O)H} + \text{OH} \rightarrow \text{C8F17C(O)OO}$	6.1×10^{-13}	0.5×10^{-13}	1
$\text{C8F17C(O)H} + \text{Cl} \rightarrow \text{C8F17C(O)OO}$	2.8×10^{-12}	0.7×10^{-12}	1
$\text{C8F17C(O)H} + \text{H2O} \rightarrow \text{C8F17CHOHOH}$	1.0×10^{-23}		1
$\text{C8F17CHOHOH} + \text{OH} \rightarrow \text{C8F17C(O)OH}$	1.22×10^{-13}	0.26×10^{-13}	1
$\text{C8F17C(O)OO} + \text{NO2} \rightarrow \text{C8F17C(O)OONO2}$	$1.1 \times 10^{-11} (298./\text{T})$	0.1×10^{-11}	3
$\text{C8F17C(O)OONO2} \rightarrow \text{C8F17C(O)OO}$	$2.8 \times 10^{16} \exp(\text{T}/-13580)$	0.2×10^{16}	3
$\text{C8F17C(O)OO} + \text{NO} \rightarrow \text{C8F17OO}$	$8.1 \times 10^{-12} \exp(\text{T}/270)$	0.6×10^{-12}	3
$\text{C8F17C(O)OO} + \text{HO2} \rightarrow \text{C8F17C(O)OH}$	$3.1 \times 10^{-13} \exp(\text{T}/1040)$	0.4×10^{-13}	3,1
$\text{C8F17C(O)OO} + \text{HO2} \rightarrow \text{C8F17OO}$	$1.2 \times 10^{-13} \exp(\text{T}/1040)$	0.4×10^{-13}	3,1
$\text{C8F17C(O)OO} + \text{CH3O2} \rightarrow \text{C8F17OO}$	$1.8 \times 10^{-12} \exp(\text{T}/500)$	3.6×10^{-13}	2
$\text{C8F17C(O)OO} + \text{CH3O2} \rightarrow \text{C8F17C(O)OH}$	$2.0 \times 10^{-13} \exp(\text{T}/500)$	$4. \times 10^{-14}$	2
$\text{C8F17OO} + \text{NO} \rightarrow \text{C8F17O}$	$2.8 \times 10^{-12} \exp(\text{T}/300.)$	1.4×10^{-13}	3
$\text{C8F17OO} + \text{HO2} \rightarrow \text{C8F17O}$	$4.1 \times 10^{-13} \exp(\text{T}/500.)$	0.4×10^{-13}	4
$\text{C8F17OO} + \text{CH3O2} \rightarrow \text{C8F17O}$	$2.7 \times 10^{-12} \exp(\text{T}/-470.)$	1.9×10^{-13}	3
$\text{C8F17OO} + \text{CH3O2} \rightarrow \text{C8F17OH}$	$1.0 \times 10^{-13} \exp(\text{T}/660)$	0.6×10^{-14}	3
$\text{C7F15C(O)F} + \text{H2O(l)} \rightarrow \text{C7F15C(O)OH}$	3.86×10^{-6}	0.7×10^{-6}	1

¹Young and Mabury [75], ²JPL Evaluation [18] using hydrocarbon analog, ³ Wallington [61], ⁴ Yarwood [72]

Table 3.2: Case environment conditions. Photochemical concentrations in cm^{-3} , temperatures in K

	Urban	Ocean	Arctic
NO	2×10^{10}	1.7×10^7	1×10^8
OH	2×10^7	5.4×10^6	1.6×10^7
NO ₂	2×10^{11}	5×10^7	1×10^8
HO ₂	9×10^6	1×10^8	3.7×10^5
RO ₂	8×10^6	1.6×10^9	2.2×10^8
$h\nu$	9.4×10^{14}	9.76×10^{14}	1×10^{15}
Temperature	299	299	265

Table 3.3: Fractional yield uncertainty contributions of rate constants (%)

Rxn #	PFOA urban	PFOA ocean	PFOA Arctic	PFNA urban	PFNA ocean	PNFA Arctic	Reaction
1	<1	<1	<1	<1	2	<1	C8F17CH2C(O)H + $h\nu$ -> C8F17CH2OO
2	<1	<1	<1	2	10	<1	C8F17CH2C(O)H + OH -> C8F17CH2C(O)OO
6	<1	<1	<1	1	2	<1	C8F17CH2C(O)OO + NO -> C8F17CH2OO
7	<1	<1	<1	1	2	<1	C8F17CH2C(O)OO + HO2 -> C8F17CH2OO
8	7	<1	<1	<1	2	<1	C8F17CH2C(O)OO + HO2 -> C8F17CH2C(O)OH
10	5	<1	<1	8	2	4	C8F17CH2C(O)OO + RO2 -> C8F17CH2C(O)OH
11	<1	<1	<1	2	2	5	C8F17CH2C(O)OH + OH -> C8F17CH2OO
12	<1	<1	<1	2	2	4	C8F17CH2C(O)OH + OH -> C8F17C(O)H
14	<1	7	<1	<1	1	27	C8F17CH2OO + NO -> C8F17CH2O
15	<1	10	<1	<1	3	<1	C8F17CH2OO + RO2 -> C8F17CH2O
16	23	48	<1	15	3	57	C8F17CH2OO + RO2 -> C8F17CH2OH
29	6	<1	<1	9	3	<1	C8F17C(O)OO + NO -> C8F17OO
30	<1	<1	<1	1	1	<1	C8F17C(O)OO + HO2 -> C8F17C(O)OH
34	5	<1	35	1	3	<1	C8F17OO + NO -> C8F17O
35	3	2	<1	3	3	<1	C8F17OO + HO2 -> C8F17O
36	<1	13	<1	2	3	<1	C8F17OO + RO2 -> C8F17O
37	8	18	63	2	1	<1	C8F17OO + RO2 -> C8F17OH

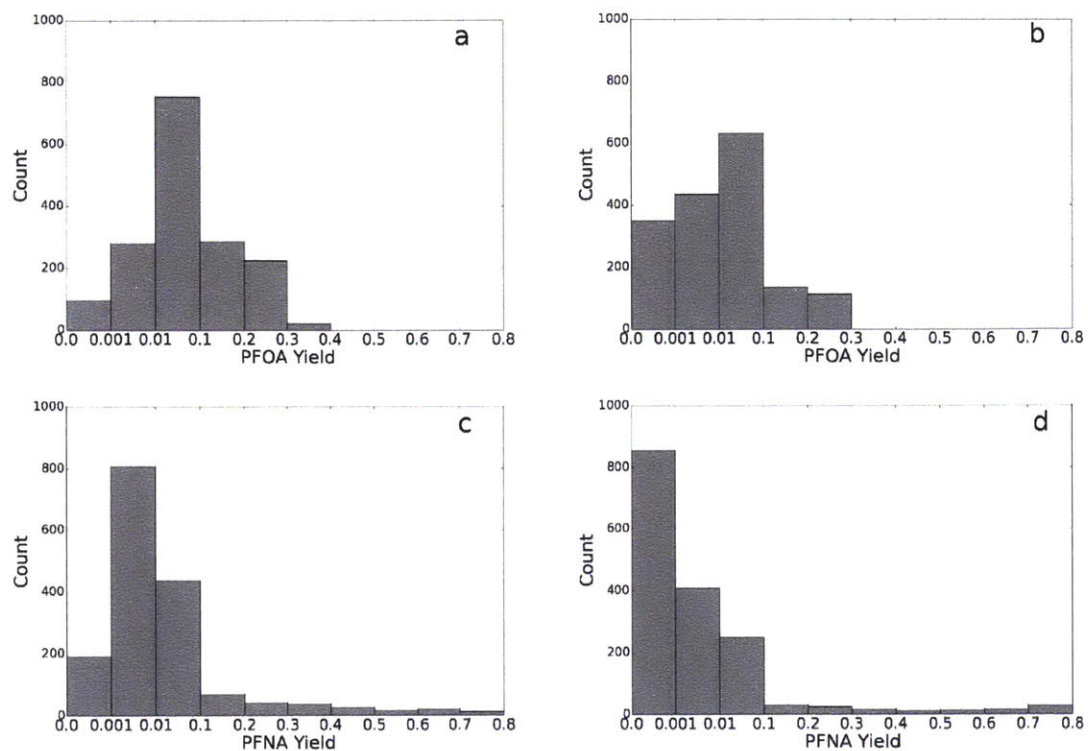


Figure 3-2: Histograms of variability in PFOA (a and b) and PFNA (c and d) theoretical maximum yields for both summer (a and c) and winter (b and d) conditions. Each count corresponds to a GEOS-Chem grid-box's output photochemical environment.

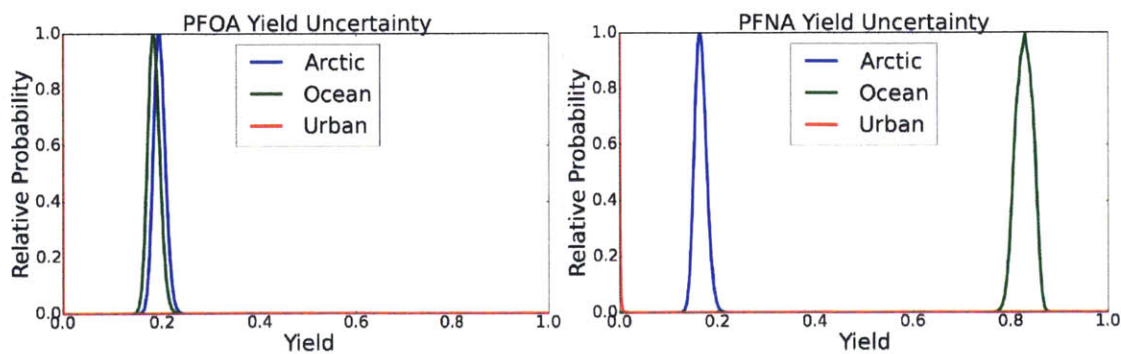


Figure 3-3: Uncertainty distributions of PFOA (left) and PFNA (right) yields for urban, ocean, and Arctic conditions. In both cases, urban yields are much less than 1%

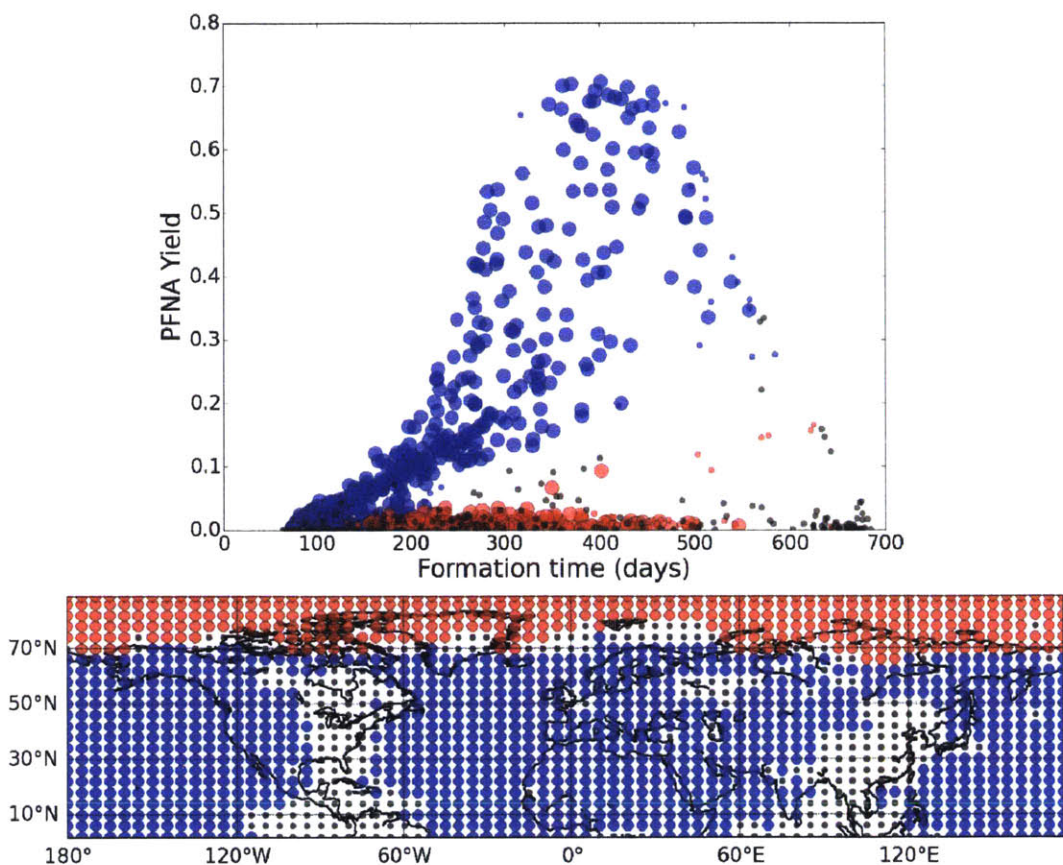


Figure 3-4: (a) Each photochemical environment plotted in yield-formation time space. Color indicates membership of a cluster in OH-HO₂-NO space. Black circles indicate unclustered points. (b) Geographic location of clusters. Colors correspond to the same clusters in both figures.

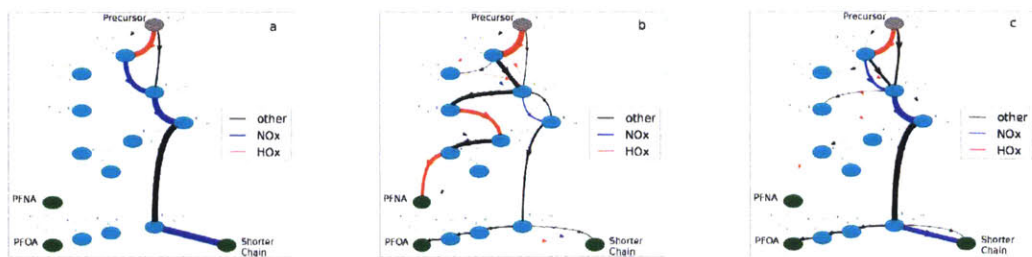


Figure 3-5: Total flux through each reaction for the degradation mechanism for urban (a), ocean (b) and Arctic (c) conditions. Each line represents a reaction, with color of the line indicating the photochemical family of the non-fluorinated reactant, and the thickness of the line is proportional to the total flux through the reaction over the course of a simulation.

Chapter 4

GEOS-Chem simulations of atmospheric PFCA formation

4.1 Abstract

Perfluorocarboxylic acids (PFCAs) are environmental contaminants that are highly persistent, bio-accumulative, and have been detected along with their atmospheric precursors far from emissions sources. The importance of precursor emissions as an indirect source of PFCAs to the environment is uncertain. Modeling studies have estimated the atmospheric source of PFCAs using models and degradation pathways of differing complexities, leading to quantitatively different results.

We present results from newly developed simulations of atmospheric PFCA formation and fate using the chemical transport model GEOS-Chem. We simulate the most up-to-date chemistry available to our knowledge for the degradation of the precursors 8:2 FTOH and fluorotelomer iodide (FTI), as well as deposition and transport of the precursors, intermediates and end-products of the formation chemistry. We find that yields of long-chain PFCAs vary greatly by geographic location and season, and that the annual response to increasing emissions is variable. We compare our model results to remote deposition measurements and find that our model reproduces Arctic deposition of PFOA effectively. We find that given the most recent precursor emission inventory [64] the atmospheric indirect source of PFOA and PFNA is 10-45 t/yr

globally and 0.2-0.7 t/yr to the Arctic.

4.2 Introduction

Perfluorocarboxylic acids (PFCAs) are persistent environmental contaminants that bio-accumulative [40, 39, 13], and, along with precursor species, have been detected far from emissions sources [73, 54, 56, 71, 49, 27]. Long-chain PFCAs (lcPFCAs) are particularly important environmentally because of the increase of detrimental effects with chain length [40, 39, 13]. Reducing lcPFCA emissions has been the intent of policy actions due to their health effects [60], resulting in decreasing direct emissions globally. Emissions of PFCA atmospheric precursors are rising [64], leading to an increasing importance in the indirect environmental source of PFCAs. Atmospheric PFCA precursors such as fluorotelomer alcohols (FTOHs) undergo photochemical reactions [15] which form PFCAs after a many-step reaction mechanism [75]. The importance of this indirect source of environmental lcPFCAs is uncertain.

Previous studies have modeled lcPFCA formation from the degradation of FTOHs in the atmosphere [72, 61]. However, studies have indicated that other emitted atmospheric precursors exist in the form of other fluorotelomer compounds [75, 64, 65, 74, 9]. The atmospheric formation of PFCAs depends on the reaction intermediate species [68, 12] with common photochemically important species, such as HO_x and NO_x . In different atmospheric environments, these species vary over orders of magnitude, affecting the ability of the atmosphere to produce lcPFCAs [Chapter 3]. This means that the connection between chemistry, transport, and deposition of PFCAs, their precursors, and intermediates in their formation, is important to the quantity of PFCA formed in the atmosphere as well as deposited to remote locations such as the Arctic. Atmospheric chemical transport models are therefore an important tool to quantifying formation and fate of PFCAs in the atmosphere.

Wallington et al. [61] simulated the atmospheric degradation of 8:2 FTOHs using the IMPACT atmospheric chemistry model. They found that PFOA yields range from 1% to 10% depending on time of year and location. Yarwood et al. [72], using

a high-resolution atmospheric chemistry model with North American coverage, estimated yields of PFOA at approximately 6% on average due to precursor degradation, and yields of PFNA of much less than 1%. Using a global-scale multispecies mass-balance model and simplified chemistry, Schenker et al. [46] found that precursor atmospheric transport followed by degradation could contribute to observed Arctic PFCAs. Previous work [Chapter 3] found using a detailed box model of updated chemistry that the capacity of the atmosphere to form PFOA and PFNA from fluorotelomer precursors in the absence of non-chemical removal varies over orders of magnitude based on location and season due to strong dependence on photochemical environment, and that in regions far from NO_x pollution sources, yields of lcPFCA can be larger than 30%.

In this work, we present results from newly developed simulations of atmospheric PFCA formation and fate using the global chemical transport model GEOS-Chem. We simulate the most up-to-date chemistry available to our knowledge for the degradation of the emitted PFCA precursors 8:2 FTOH and fluorotelomer iodide (FTI), as well as deposition and transport of the precursors, intermediates and end-products of the degradation chemistry. We find that yields of lcPFCAs vary greatly by geographic location, and that the annual response to increasing emissions is variable. We compare our model results to remote deposition measurements and find that our model reproduces Arctic deposition of PFOA effectively. We find that given the most recent precursor emissions inventory [64], the atmospheric indirect source of PFOA and PFNA is 10-45 t/yr globally and 0.2-0.7 t/yr to the Arctic.

4.3 Materials and Methods

We introduce GEOS-Chem simulations of the atmospheric chemistry that leads to atmospheric PFCA formation and the transport and fate of precursor, intermediate and PFCA species. We use the GEOS-Chem model [4] framework to simulate the transport and fate of fluorotelomer precursors, from their chemical degradation to their deposition and the deposition of their reaction products. We build on estab-

lished GEOS-Chem simulations of atmospheric photochemistry for reliability and to facilitate future atmospheric PFCA modeling work.

4.3.1 PFCA formation chemistry model

In our model, we use the precursor degradation mechanism from [Chapter 3] which builds on the work of previous modeling efforts [61, 72] with additional reactions from more recent literature [75]. The chemical reactions included are listed in Table 3.6. The mechanism defines the degradation of 8:2 FTOH and 8:2 FTI, which are the most commonly emitted fluorotelomer PFCA precursors [64], to form FT-aldehyde and further intermediate and stable end products including PFOA and other PFCAs. The FT-aldehyde can be oxidized by OH or photolyzed to form peroxy and acylperoxy radicals. These radicals react with NO, NO₂, RO₂, and HO₂ to form intermediates which can again be radicalized by OH and ultraviolet light, with further radical reactions leading to stable PFCAs or intermediates with reduced chain length. Reaction products which have chain lengths shorter than PFHxA (6 Carbons) are aggregated in our model.

We add the fluorotelomer degradation chemistry to the existing GEOS-Chem v10.01 full chemistry simulation, which calculates the concentrations of HO_x, NO_x, RO₂, etc. on a global Eulerian grid using a detailed set of chemical reactions, detailed emissions inventories, prescribed meteorology from GEOS-5 reanalysis, and wet and dry deposition schemes. This combination of GEOS-Chem photochemistry with the fluorotelomer degradation mechanism at a relatively high spatial resolution of 4°x5° provides a detailed representation of the temporal and spatial variability in atmospheric PFCA formation, which is important in estimating the atmospheric source of PFCA to remote regions [Chapter 3].

Due to the solubility of PFCAs and some of the intermediates in their formation, wet deposition and scavenging is an important non-chemical removal process to account for in our simulations. For wet removal, we use a scheme analogous to that for existing soluble GEOS-Chem species such as H₂O₂. Wet removal can occur as rainout and washout from both large-scale and convective precipitation, as well as

scavenging in updrafts. Fluorinated species in the model are found in liquid water according to their Henry's Law constants. We calculate Henry's Law coefficients using the Henrywin application in the EPISUITE software package, which uses a group additive method for estimating physicochemical properties of species for which experimental determinations are unavailable. For some highly fluorinated species, including FTOHs, this method can be highly inaccurate [1]. Different methods of estimation give Henry's Law constants differing by multiple orders of magnitude, and the effect of these uncertainties should be investigated in future work.

For emissions of 8:2 FTOH and FTI, we use the inventory of Wang et al. [64] which gives total fluorotelomer production estimates for the period 1962 to present, and a constant estimate of the non-polymer C8 homologue fraction, which we use to calculate annual release of 8:2 fluorotelomer precursor. We assume that released precursor is 90% FTOH and 10% FTI. The inventory gives constant average annual emissions for groups of years, and we interpolate these average values to result in smooth changes between years while conserving the inventory's total cumulative emissions. We assume that the spatial distribution of emissions due to use and disposal of fluorotelomer products is the same as the anthropogenic emissions of NO_x over land. This results in a pattern of emissions similar to those of Stemmler and Lammel [55] who weighted their emissions by GDP.

Simulations are conducted for years 2004-2012 with 2004 used twice, once as a spin-up year.

4.3.2 Comparison to observations

We compare our model output 8:2 FTOH concentrations as well as PFOA and PFNA depositions at remote sites to measurements of these quantities. Gas-phase FTOH concentrations were measured over the period 2004-2006 on Cornwallis Island in the Canadian Arctic [56], on a cruise from Europe to the Canadian Arctic Archipelago [54] and in the city of Toronto [54] by high volume air samplers. We compare these measurements to monthly average modeled concentrations for the months in which the measurements were conducted. PFOA and PFNA annual deposition fluxes were

measured [73] for the years 2004 and 2005 at a collection of ice caps in the Arctic Archipelago by analyzing snow samples. We directly compare our annual deposition fluxes for each of these years to the fluxes measured. In both comparison cases, we include a "representativeness error" [58] in the measurements which estimates the effect of comparing a point measurement to a model grid-box using the local spatial variability in the model output.

4.4 Results

4.4.1 Measurement comparison at remote sites

Figure 4-1 shows measured and modeled concentrations of 8:2 FTOH for the locations described above. The error bars on the measurements indicate statistical variability over the measurement period and representativeness error. Model concentrations of 8:2 FTOH agree within uncertainty for the remote high-latitude measurement sets. In both the Cornwallis Island and cruise cases, model mean concentration is lower than measured mean concentration, but the variability ranges overlap significantly. This lends confidence to the model's ability to simulate the fate of 8:2 FTOH in - and transport to - the Arctic environment. In the case of the Toronto measurements, model concentrations are significantly lower than the observed values. This could be due to differences in spatial distributions of emissions in our model compared to reality or it could be the dilution effect of a relatively large model grid box compared to a smaller scale city source.

Figure 4-2 shows the model-measurement comparison for deposition to four ice caps in the Canadian Arctic Archipelago. Each bar is the annual deposition flux for each ice cap for the years 2004 and 2005. The error bars for the measurements represent the representativeness errors for the model-measurement comparison. The figure shows that the model captures the deposition of PFOA at the Arctic sites well, with the single exception being deposition to the Devon Ice Cap in 2005. Figure 4-3 shows the same comparison, this time for PFNA. In simulating PFNA deposition,

the model performs less well than for PFOA. Across all site and years, the model flux is lower than the observed flux, although in some cases within the error bars. This discrepancy could be due to PFNA formation pathways that are unrepresented in the model. A sensitivity test was performed for one of these proposed mechanisms, the gas-phase formation of perfluoroaldehyde hydrate from reaction of perfluoroaldehyde and water vapor. The model error bars on figure 4-3 show the simulated deposition flux including this reaction with the rate constant at the upper limit deduced by experiment [75]. Using this extra reaction, model fluxes are increased to agree better with the observations. Even in this sensitivity test, Devon Ice Cap measured PFNA deposition is much higher than the model's deposition in 2005, much like PFOA.

4.4.2 Deposition of PFCAs

Figure 4-4 shows the spatial distribution of PFOA deposition globally. While total deposition is considered below, dry deposition is much smaller than wet deposition globally and wet deposition drives the spatial patterns and deposition magnitudes discussed. Deposition rates vary across orders of magnitude globally, due to both variations in PFOA formation and rates of precipitation, as wet deposition is very important for PFCAs. The highest deposition rates occur near the equator, especially in the region of the Intertropical Convergence Zone (ITCZ). This is likely due to the high rates of precipitation in this region. The other highest deposition rates occur over the oceans downstream of strong emissions sources such as Eastern North America and Eastern Asia. Desert areas show very little deposition, highlighting the importance of rain and wet removal for PFCAs. Figure 4-5 shows the same information for PFNA deposition. Across the globe, PFNA shows a very similar spatial pattern to PFOA with lower magnitudes of deposition. Farther from the equator and emissions sources, the ratio of PFOA to PFNA deposition gets closer to 1, highlighting the relationship between PFNA yield and formation time discussed in previous work [Chapter 3].

Over North America, we see largely the same spatial pattern of PFOA as [72], with the highest values over the Eastern U.S. and decreasing deposition westward and northward. PFNA deposition follows a very similar pattern to PFOA with lower

magnitude for both [72] and this study. In this study we see a faster downstream decrease in deposition, possibly due to the fact that we do not include direct emissions of PFCAs, which have a source in the Eastern United States.

Figure 4-7 shows global total PFOA and PFNA deposition as a function of time for the period of available GEOS-5 meteorology. In each year, PFOA deposition is substantially greater than PFNA deposition. Both PFOA and PFNA show a generally increasing trend across the time-period, driven by increasing precursor emissions globally [64]. While the emissions are effectively linearly increasing, deposition of PFOA and PFNA are not. The year-to-year variability from the average trend is driven by variability in precipitation, particularly in the regions of high deposition fluxes that drive the total, and by variability in atmospheric PFCA formation caused by year-to-year variations in photochemical environment. Figure 4-6 shows much of the same behavior in total Arctic deposition, with more inter-annual variability and more similar magnitudes of PFOA and PFNA deposition.

Wallington et al. [61] estimated 0.4 tonnes per year PFOA deposition to the Arctic using the upper limit of available emissions estimates. This falls within the range of deposition that we calculate using maximum and minimum emissions scenarios. Wania [66] estimated with a zonally averaged transport model 150 kg per year deposited to the Arctic because of atmospherically generated PFCAs. This corresponds to our lower bound of PFOA deposition to the Arctic.

4.4.3 Yields of PFCAs

Figures 4-8 and 4-9 show the fraction of total fluorinated compound deposition accounted for by each of PFOA and PFNA, respectively, for each GEOS-Chem grid box. This value is on average 5% globally for PFOA and 2% globally for PFNA. Close to NO_x sources, this value is on the order of 1% or lower for PFOA and much less than 1% for PFNA. This demonstrates the reduced capacity for NO_x -polluted atmospheres to form PFCAs from precursors [75],[Chapter 3]. Farther from sources, PFOA makes up 10% or more of deposited fluorinated material, peaking at close to 60% near Antarctica. The PFNA fraction remains low except very far from sources,

in the Canadian Arctic and Southern Ocean, where it rises above 10%.

Wallington et al.'s [61] model predicted that the highest PFOA fractions would occur over the equatorial oceans and Southern Ocean. We find largely the same patterns, with quantitative differences in both larger maximum and smaller minimum fractions contributed by PFOA. Yarwood et al. [72] calculate annual yields of 0.84% PFOA and 0.22% PFNA over the U.S. which are in agreement with our model results.

4.5 Discussion

Our model simulations compare well with measured values for both remote FTOH concentrations and deposition of PFCAs. While the model appears to capture the production and deposition of PFOA very well, the source of PFNA to the Arctic sites is underestimated compared to observations. By including a gas-phase perfluorinated aldehyde (PFAL) hydration reaction using the experimentally determined upper limit of its reaction rate [75] we can account for this PFNA underestimation without affecting the PFOA agreement. Since this represents the upper limit of PFNA formation through the gas-phase hydration mechanism, the actual PFNA production by this pathway is likely smaller. Another possible hydration pathway is the heterogeneous hydration of PFAL, which is not resolved in the current version of the model. With better experimental determinations of the gas-phase and heterogeneous hydration of PFAL, and the inclusion of both in future iterations of this model, the atmospheric source of PFNA could be better quantified.

We consider here the degradation of 8:2 FTOHs and FTIs, but PFOA and PFNA can also be formed through the degradation of 10:2 and larger precursor molecules, analogously to how PFHpA and PFHxA are formed in our model. While this would have a quantitative impact on our predicted PFOA and PFNA deposition rates, 10:2 and higher homologues of FT-species are emitted in much smaller quantities than their 8:2 and shorter counterparts [64]. Fluorotelomer species other than alcohols and iodides are also emitted, but how small a fraction of the fluorotelomer total they compose is uncertain. While we neglect them in the current study, the slightly

different chemistry of fluorotelomer olefins, for instance, could yield more PFCA per unit emission than FTOHs and FTIs due to their initial degradation reaction. Future consideration of these species could be important if they are found to be emitted in non-negligible quantities compared to FTOHs.

Previous modeling work [61] estimated the atmospheric indirect source of PFOA to the Arctic using a chemical transport model for a representative year with hypothetical emissions. While the chemistry simulated by that model was the most detailed of its time, it did not include the complete set of reactions used by our model. The hypothetical emissions scenario used in that study is above more recent emissions estimates [64], but their model predicts Arctic deposition which agrees with our upper limit estimates for the years 2004-2007. For the comparison to measurements that we make, it is important that we used time-resolved estimates of emissions corresponding to specific meteorological years to properly assess the performance of our model, which previous global scale atmospheric modeling has not had the opportunity to do.

A more detailed chemistry including most of our model's reactions was included in a regional scale modeling study [72] which focused on North American impacts of atmospherically formed PFCAs, but the effect on the rest of the Northern Hemisphere was estimated in an average sense. Given the diversity of PFCA formation across the Northern Hemisphere [Chapter 3] and the spatial differences we see across the European Arctic, as well as the deposition of atmospherically formed PFCAs to the Southern Ocean, having global coverage in our model is an asset to quantifying both Arctic and global sources of PFCAs.

Globally, approximately 5% of the deposited products of fluorotelomer releases are PFOA. At lower latitudes, this number is commonly between less than 1% and 10%, but over the Southern Ocean, this number climbs above 50% in places. Similarly, PFNA makes up much less than 1% of the deposited products at low latitudes but more than 10% over the Southern Ocean. While fluxes of PFCAs are lower at these southern latitudes, the longer chain PFCAs of more consequence make up a much higher fraction.

Our work demonstrates the importance of remote measurements of quantities that

can be predicted by models, such as total deposition of long-chain PFCAs. Based on our results, and given the declining importance of direct emissions of long-chain PFCAs, the signal of atmospherically produced PFCAs in the future should be easily detectable in the precipitation of the tropics. Sites that are both remote and tropical such as Pacific islands see high annual deposition rates which could be observed through measurements of PFCAs in precipitation. We also see in our model results varying relative abundances of different PFCA homologues in deposition in different regions, meaning that measurement of many members of the homologue series in a single location is a valuable dimension for model validation.

We assume a spatial distribution of emissions which is correlated with NO_x emissions. Given the relationship of reduced yields of longer chain PFCAs under higher NO_x conditions [75, 61],[Chapter 3], this assumption will lead to lower modeled atmospheric production of long-chain PFCAs than an emissions distribution which is less correlated with NO_x emissions. With that said, we believe that this assumption, which leads to similar distributions as previous estimates [55], is reasonable.

Using the most up-to-date chemistry available to our knowledge for the degradation of PFCA precursors, we find that our model results compare well to remote deposition measurements and reproduce Arctic deposition of PFCAs effectively. The simulations of atmospheric PFCA formation and fate that we introduce in the GEOS-Chem model framework can be used in future work to investigate further elements of atmospheric PFCA formation, such as yet-unstudied gas-phase and heterogeneous reactions, future emissions scenarios, and uncertainty in the spatial distribution of emissions.

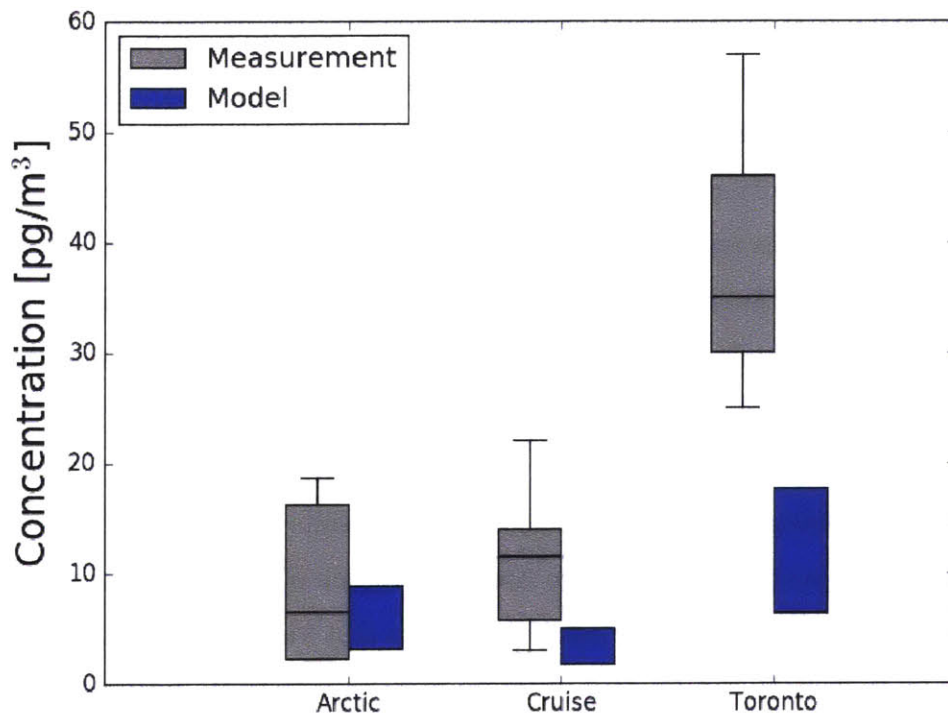


Figure 4-1: Measurement-model comparison for 8:2 FTOH concentrations at two remote and one urban location. The gray boxes represent the median and the lower and upper quartiles of the measurement data, with whiskers extending to the full range of the measurements. The blue boxes represent the model range between maximum and minimum emissions scenarios.

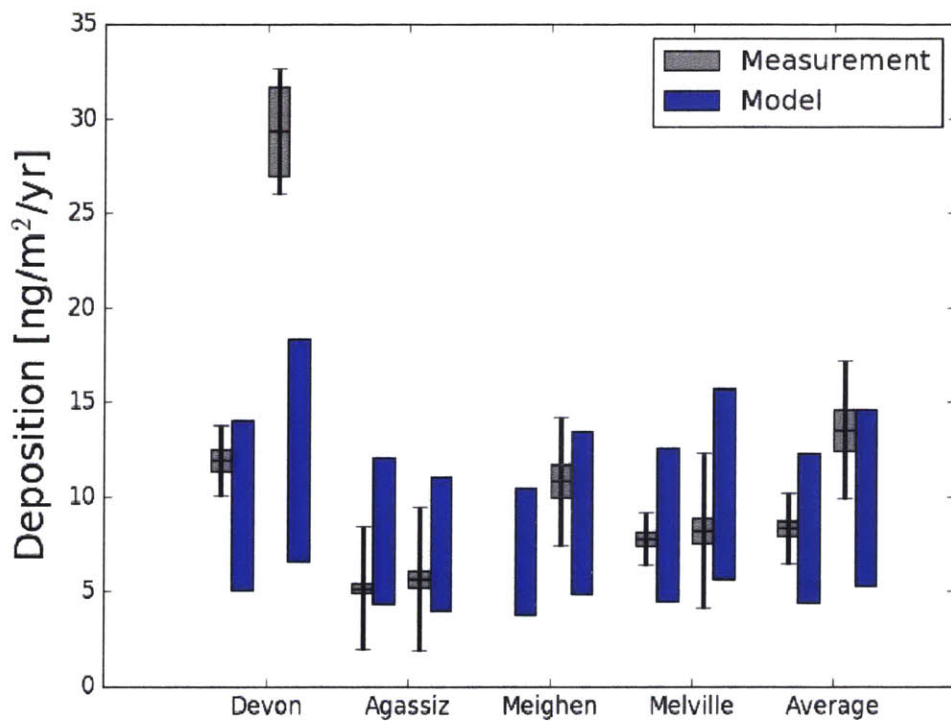


Figure 4-2: Measurement-model comparison for PFOA deposition for 2004 (first bars) and 2005 (second bars) at four Canadian ice caps. The gray boxes represent the measurement uncertainty, with error bars representing the error from comparing a point measurement to model grid-box. The blue boxes represent the model range between maximum and minimum emissions scenarios.

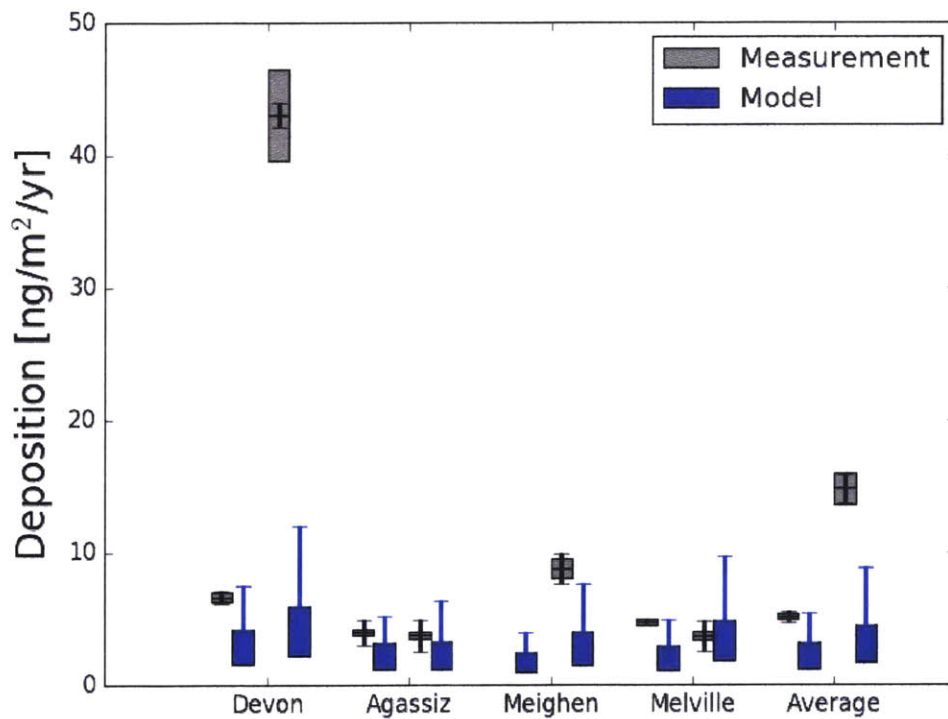


Figure 4-3: Measurement-model comparison for PFNA deposition for 2004 (first bars) and 2005 (second bars) at four Canadian ice caps. The gray boxes represent the measurement uncertainty, with error bars representing the error from comparing a point measurement to model grid-box. The blue boxes represent the model range between maximum and minimum emissions scenarios, with the blue error bar representing the perfluorinated aldehyde hydration sensitivity test.

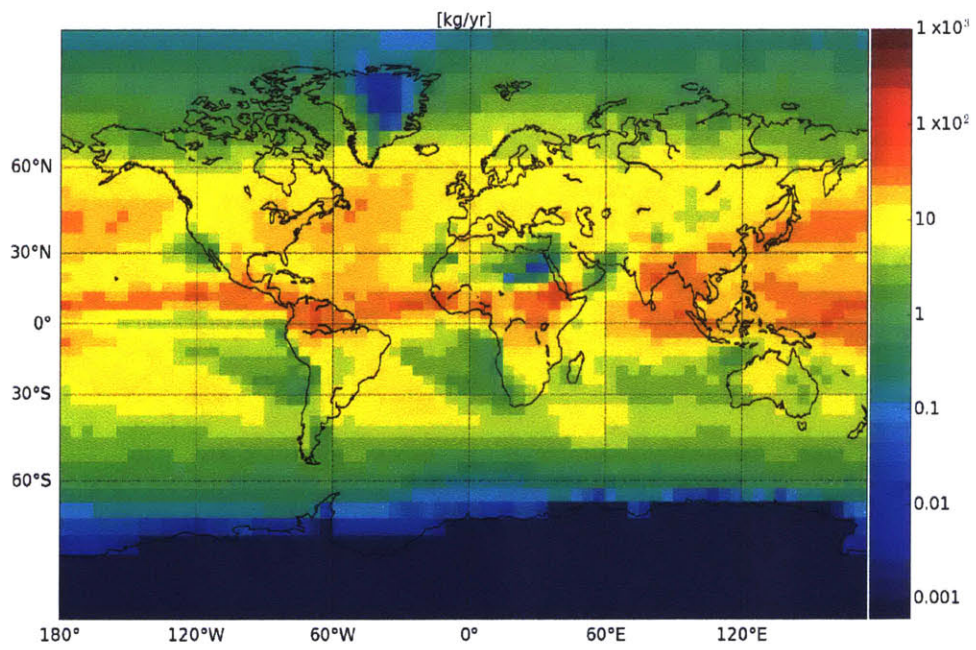


Figure 4-4: Spatial distribution of PFOA deposition (kg/yr) in each GEOS-Chem grid-box.

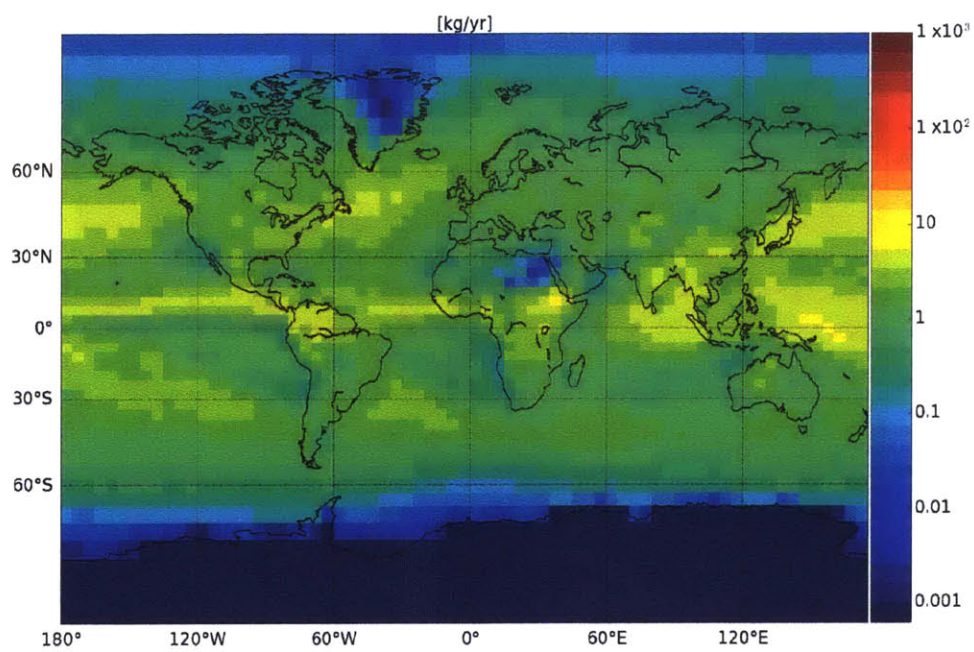


Figure 4-5: Spatial distribution of PFNA deposition (kg/yr) in each GEOS-Chem grid-box.

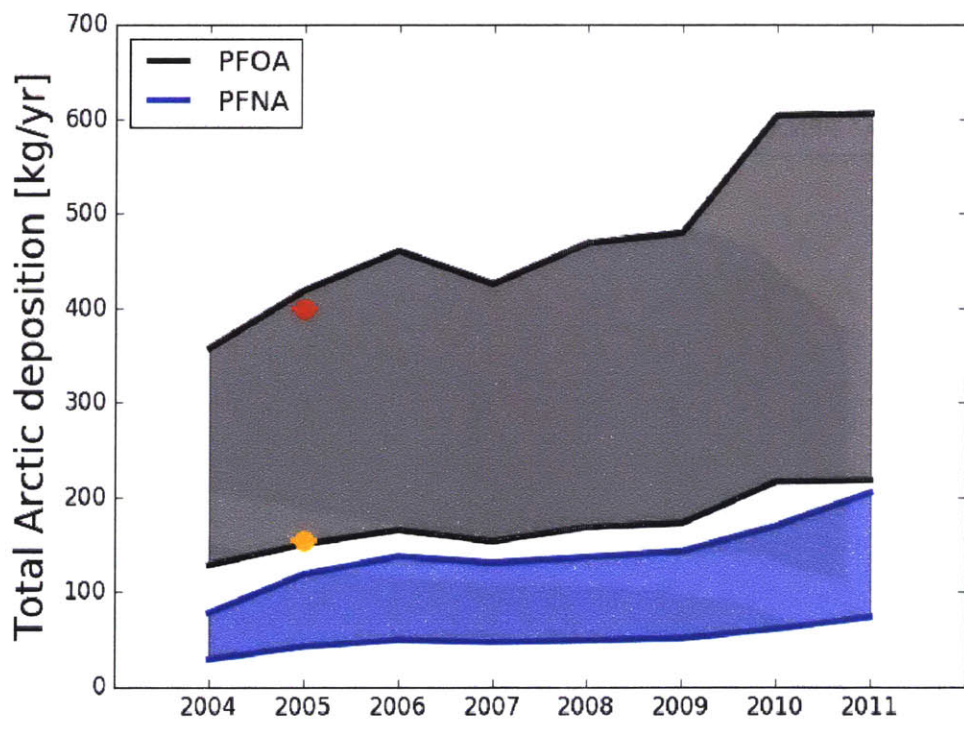


Figure 4-6: Time series of annual total Arctic deposition of PFOA (gray) and PFNA (blue). Orange mark corresponds to Wania [66] estimate and red mark corresponds to Wallington [61].

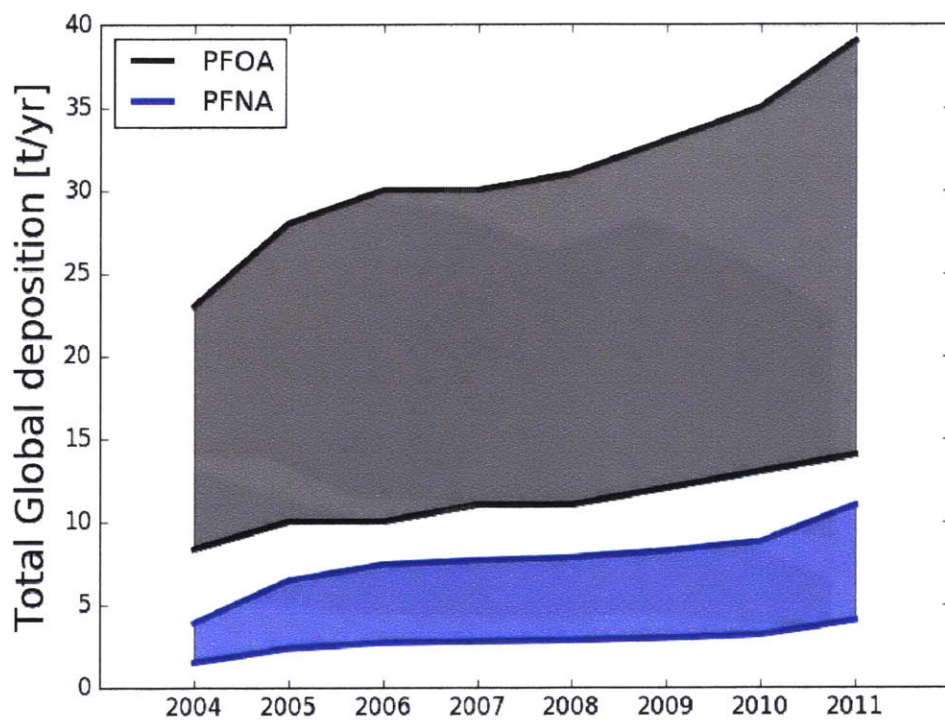


Figure 4-7: Time series of annual total Arctic deposition of PFOA (gray) and PFNA (blue).

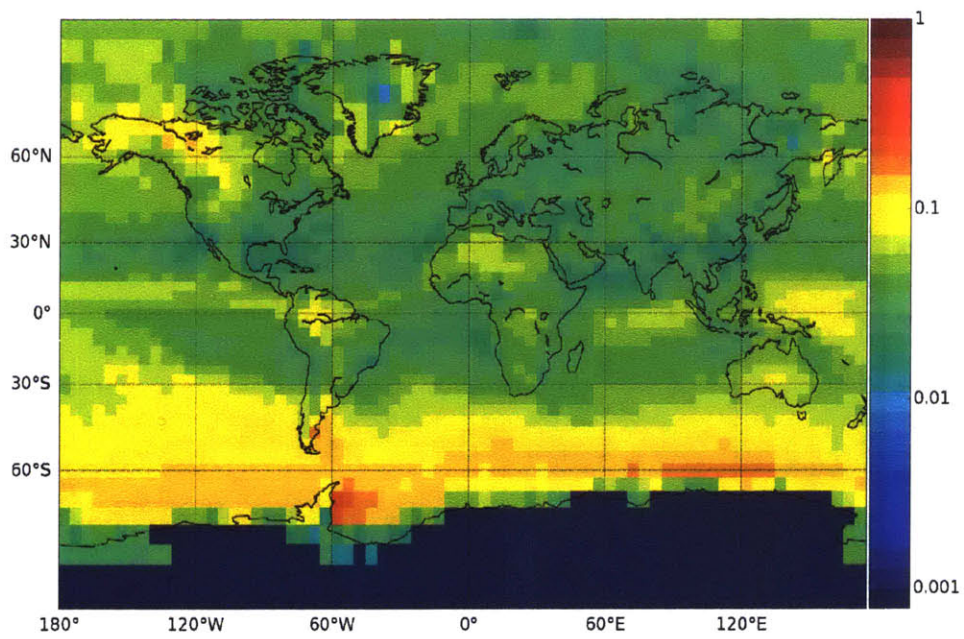


Figure 4-8: Spatial distribution of the PFOA fraction of total deposition of fluorinated species.

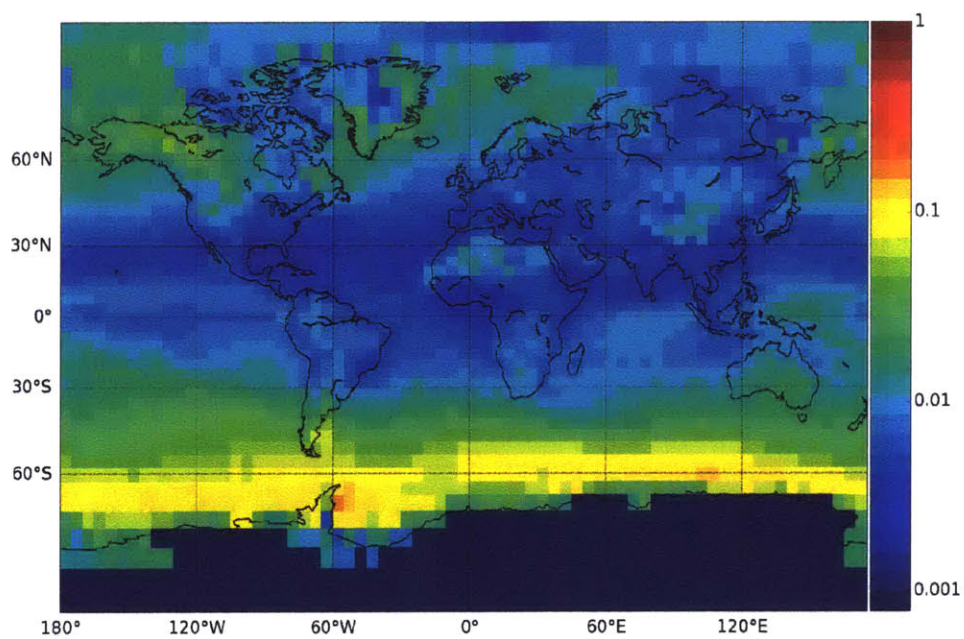


Figure 4-9: Spatial distribution of the PFNA fraction of total deposition of fluorinated species.

Chapter 5

Conclusion

In this thesis, I have studied two classes of POPs: PAHs and PFCAs. Using the GEOS-Chem atmospheric chemical transport model and polynomial chaos expansions, I have quantified and highlighted uncertainties in our simulations of POPs in the atmosphere, as well as pinpointed where future experiments could reduce our uncertainty the most. By developing new GEOS-Chem simulations of PFCA formation, future research concerning the atmospheric formation and transport of PFCAs has something to easily build on.

In Chapter 2, I quantified the uncertainty in GEOS-Chem PAH simulations that stems from uncertain model inputs such as physicochemical properties and emissions estimates. I found that the hydroxyl reaction rates were the leading contributors to uncertainty, and used measurements along with uncertainty information to better constrain the model inputs leading to uncertainty. In Chapter 3, I investigated atmospheric PFCA formation from emitted precursors using a box model driven by GEOS-Chem outputs. I quantified the variability in PFCA yields in different atmospheric environments, and the uncertainty in these yields. In Chapter 4, I introduced simulations of PFCA formation in GEOS-Chem itself. The simulations agreed well with remote measurements of concentrations and deposition. I calculated global and Arctic fluxes of PFCAs due to atmospheric formation and transport, and found that they are 10-45 t/yr and 0.2-0.7 t/yr, respectively.

In Chapter 2, I used the combination of measurements and model results to re-

duce uncertainty in hydroxyl reaction rate constants and emissions magnitudes. This highlights the dual importance of both global scale models and consistent measurements at remote locations. Measurements at remote sites can act qualitatively or quantitatively to ground modeling work to measurable quantities, and global models can fill in the gaps between point measurements. The combination of both can lead to a global model whose predictions are optimized to reflect the measurements, and thereby fill in the temporal and spatial measurement gaps optimally as well.

In Chapters 2 and 3, my uncertainty analysis singles out some important sources of uncertainty, parameters whose experimental determination would have the greatest power to reduce uncertainty in model results. In the case of PAHs, the rate constants for gas phase reactions between PAHs and OH radicals contribute the majority of uncertainty for phenanthrene and pyrene and contribute significantly for benzo[a]pyrene. For pyrene and benzo[a]pyrene, these rate constants have only been estimated using highly uncertain theoretical methods, and any experimental determination would greatly reduce uncertainty in these important model inputs. Phenanthrene's OH rate constant has been measured, but improved precision of this measurement would provide the largest gains for model output uncertainty for phenanthrene because it is predominantly in the gas phase. For benzo[a]pyrene, gas-particle partition coefficients are also important contributors to uncertainty, as this PAH has a high affinity to black carbon particulate matter. Reducing the error bars on this partitioning would greatly reduce model benzo[a]pyrene uncertainty. In the case of PFCA formation, many reactions' rate constants have yet to be quantified experimentally, but according to our analysis, the key rate constants for reducing uncertainty in quantities of formed PFCAs are those corresponding to fluorinated peroxy radical reactions that are branching points in the chemical mechanism. The relative rates of these reactions determine, in general, what fraction of reactant gets its chain length shortened, leading to shorter chain products. Measurements of these rate constants, or even relative rate measurements for the reactions at these branching points, would reduce model uncertainty.

The combination of long-term measurements at remote sites with a global model

can have important benefits for modelers, as shown in Chapter 2, but my modeling uncertainty analysis can also inform future measurements. I found, through sensitivity tests with the PCEs of the GEOS-Chem PAH simulations, that the places where future measurements could best constrain what we know about PAHs in the atmosphere are far from sources in the remote Southern Hemisphere. These locations, however, also tend to have the lowest concentrations of PAHs, making them locations where long-term measurements of the types performed in the Northern Hemisphere would be most difficult to conduct. Measurements at these remote Southern Hemisphere sites could sacrifice temporal resolution for more accurate determinations of longer-term average PAH concentrations that are very small. This would be the most effective way of constraining the important physicochemical properties of PAHs in a top-down manner, and combined with the above-mentioned experimental determinations of these properties, the very large uncertainties associated with atmospheric PAH modeling could be greatly reduced. For example, long-term monitoring of atmospheric constituents already happens at Cape Grimm in Australia. Adding PAH monitoring to this existing station could be an achievable first step in Southern Hemisphere PAH measurements.

My GEOS-Chem modeling of PFCA formation tells a similar story regarding where measurements could best be performed. Long-term measurements at remote sites are best for constraining the chemistry that leads to long-chain PFCAs, and in particular measurements of multiple PFCA homologues can better validate our knowledge of the mechanism of PFCA formation. I found, for instance, that the ratio of 8 carbon PFOA to 9 carbon PFNA deposited annually in precipitation had a latitudinal dependence, with much more PFOA at lower latitudes, and the ratio getting closer to unity moving pole-ward. Long-term measurements at remote sites at different latitudes could be used to validate these results, and would be important to future model-measurement comparisons. The GEOS-Chem simulations shown in Chapter 4 also are characterized by large deposition rates in precipitation in the tropics. These areas experience large amounts of precipitation, but no measurement studies have sampled these regions for PFCA deposition over long periods of time. As

PFCA fluxes are orders of magnitude higher in the tropics than the Arctic according to the GEOS-Chem results, such measurements would be important for constraining the global budget of atmospherically produced PFCAs.

In Chapter 2, I establish that due to the orders-of-magnitude differences in photochemical species concentrations in different atmospheric environments, the uncertainty due to rate constant uncertainty at given conditions is secondary to the variability in conditions that an air parcel experiences as it is transported through the atmosphere. Therefore, it is important to be able to capture this variability to effectively model the atmospheric formation of PFCAs, meaning that CTM simulations are necessary to properly resolve PFCA formation. Previous studies have either included most of the necessary details but been constrained to regional scale, or have used a global model with many simplifying assumptions. The benefits of using the GEOS-Chem framework for modeling PFCA formation are many. For one, it is global scale and after the work of Chapter 4, includes the detailed representation of PFCA formation chemistry. This global scale is important due to the diversity of PFCA formation environments and the differences in deposition rates that we see across regions of the globe. Secondly, it is a community model which has many groups working to improve many aspects of the model outside of the particulars of PFCA formation chemistry. Any improvements to other elements of the model are easily transferred to PFCA simulations so that future work could benefit from these improvements without explicit effort. GEOS-Chem also benefits from having an adaptable emissions inventory system which means that future estimates of emissions important to PFCA formation can be seamlessly folded in to the simulations with very little effort. Since GEOS-Chem is driven by reanalysis meteorology, it can be used to compare to specific measurements in time and space and capture episodic behavior in chemistry and transport. This is important for capturing both inter-annual variability and seasonal- or shorter-scale variability in both predicted fluxes of PFCAs from the atmosphere and accurate comparisons to observations. Finally, work has already been done to couple GEOS-Chem deposition outputs from the atmosphere to an ocean model for POPs, meaning that work to model the entire atmosphere-ocean system for PFCAs

is a possible next step.

Future emissions of long-chain PFCA precursors are hoped to be controlled by programs such as the EPA Stewardship program. Compliance with this program by emitters of fluorotelomer compounds would greatly limit the atmospheric production of long-chain PFCAs. It is doubtful, however, that the growing Asian fluorotelomer industry will be in compliance with this Stewardship program, and global fluorotelomer emissions will likely continue to increase in the near term even if Western sources see a sharp decline. Given that we calculate that globally, 5% of emitted 8:2 fluorotelomer precursors are deposited as PFOA, rising precursor emissions could eventually return atmospheric PFOA to pre-reduction levels. Programs to curb long-chain precursor emissions are therefore necessary on a global level to ensure the eventual decline of PFOA in the environment.

Bibliography

- [1] H. P. H. Arp, C. Niederer, and K.-U. Goss. Predicting the partitioning behavior of various highly fluorinated compounds. *Environ. Sci. Technol.*, 40:7298–7304, 2006.
- [2] Roger Atkinson. Kinetics and mechanisms of the gas-phase reactions of the hydroxyl radical with organic compounds. *J. Phys. Chem. Ref. Data*, Monograph 1:1–246, 1989.
- [3] H. Barring, T. D. Bucheli, D. Broman, and O. Gustafsson. Soot-water distribution coefficients for polychlorinated dibenzo-p-dioxins, polychlorinated dibenzofurans and polybrominated diphenylethers determined with the soot cosolvency-column method. *Chemosphere*, 49(6):515–523, 2002. 604QD CHEMOSPHERE.
- [4] I. Bey, D. J. Jacob, R. M. Yantosca, J. A. Logan, B. Field, A. M. Fiore, Q. Li, H. Liu, L. J. Mickley, and M. Schultz. Global modeling of tropospheric chemistry with assimilated meteorology: Model description and evaluation. *J. Geophys. Res.*, 106:23073–23096, 2001.
- [5] H.W. Biermann, H. Mac Leod, R. Atkinson, A.M. Winer, and J.N. Pitts. Kinetics of the gas-phase reactions of the hydroxyl radical with naphthalene, phenanthrene, and anthracene. *Environ. Sci. Technol.*, 19:244–248, 1985.
- [6] Paolo Boffetta, Nadia Jourenkova, and Per Gustavsson. Cancer risk from occupational and environmental exposure to polycyclic aromatic hydrocarbons. *Cancer Causes & Control*, 8(3):444–472, 1997.
- [7] T.C. Bond, E Bhardwaj, R Dong, R Jogani, S Jung, C Roden, D.G. Streets, and N.M. Trautmann. Historical emissions of black and organic carbon aerosol from energy-related combustion, 1850-2000. *Global Biogeochem. Cycles*, 21:GB2018, 2007.
- [8] W. W. Brubaker and R. A. Hites. OH reaction kinetics of polycyclic aromatic hydrocarbons and polychlorinated dibenzo-p-dioxins and dibenzofurans. *J. Phys. Chem. A*, 102:915–921, 1998. YW472 J PHYS CHEM A.
- [9] C. M. Butt, C. J. Young, S. A. Mabury, M. D. Hurley, and T. J. Wallington. Atmospheric chemistry of 4:2 fluorotelomer acrylate (c4f9ch2ch2oc(o)ch=ch2): kinetics, mechanisms and products of chlorine atom and oh radical initiated oxidation. *J. Phys. Chem. A*, 113:3155–3161, 2009.

- [10] Yu-Han Chen and Ronald G. Prinn. Estimation of atmospheric methane emissions between 1996 and 2001 using a three-dimensional global chemical transport model. *J. Geophys. Res.*, 111(D10):27, 2006.
- [11] H. Cheng and A. Sandu. Uncertainty quantification and apportionment in air quality models using the polynomial chaos method. *Environ. Model. Softw.*, 24:917–925, 2009.
- [12] M. S. Chiappero, F. E. Malanca, G. A. Arguello, S. T. Wooldridge, M. D. Hurley, J. C. Ball, T. J. Wallington, R. L. Waterland, and R. C. Buck. Atmospheric chemistry of perfluoroaldehydes ($\text{C}_x\text{F}_{2x+1}\text{CHO}$) and fluorotelomer aldehydes ($\text{C}_x\text{F}_{2x+1}\text{CH}_2\text{CHO}$): Quantification of the important role of photolysis. *J. Phys. Chem. A*, 110:11944–11953, 2006.
- [13] J. M. Conder, R. A. Hoke, W. de Wolf, M. H. Russell, and R. C. Buck. Are pfcas bioaccumulative? a critical review and comparison with regulatory criteria and persistent lipophilic compounds. *Environ. Sci. Technol.*, 42:995–1003, 2008.
- [14] J. Dachs and S. J. Eisenreich. Adsorption onto aerosol soot carbon dominates gas-particle partitioning of polycyclic aromatic hydrocarbons. *Environ. Sci. Technol.*, 34:3690–3697, 2000. 349RQ ENVIRON SCI TECHNOL.
- [15] D. A. Ellis, J. W. Martin, S. A. Mabury, M. D. Hurley, M. P. S. Andersen, and T. J. Wallington. Atmospheric lifetime of fluorotelomer alcohols. *Environ. Sci. Technol.*, 37:3816–3820, 2003.
- [16] M. Ester, H-P Kriegel, J. Sander, and X. Xu. A density-based algorithm for discovering clusters in large spatial databases with noise. pages 226–231. AAAI Press, 1996.
- [17] K. Fenner, M. Scheringer, M. MacLeod, M. Matthies, T. McKone, M. Stroebe, A. Beyer, M. Bonnell, A. C. Le Gall, J. Klasmeier, D. Mackay, D. Van De Meent, D. Pennington, B. Scharenberg, N. Suzuki, and F. Wania. Comparing estimates of persistence and long-range transport potential among multimedia models. *Environmental Science & Technology*, 39(7):1932–1942, 2005.
- [18] NASA Panel for Data Evaluation. Chemical kinetics and photochemical data for use in atmospheric studies, 2015.
- [19] Carey L. Friedman and Noelle E. Selin. Long-Range Atmospheric Transport of Polycyclic Aromatic Hydrocarbons: A Global 3-D Model Analysis Including Evaluation of Arctic Sources. *Environ. Sci. Technol.*, 46(17):9501–9510, September 2012.
- [20] C.L. Friedman, J.R. Pierce, and N.E. Selin. Assessing the influence of secondary organic aerosols on long-range atmospheric PAH transport. *Environ. Sci. Technol.*, Submitted, 2013.

- [21] C.L. Friedman, Y. Zhang, and N.E. Selin. Climate change and emissions impacts on atmospheric PAH transport to the Arctic. *Environ. Sci. Technol.*, 48:429–437, 2014.
- [22] E. Galarneau, P.A. Makar, Q. Zheng, J. Narayan, J. Zhang, M.D. Moran, M.A. Bari, S. Pathela, A. Chen, and R. Chlumsky. PAH concentrations simulated with the AURAMS-PAH chemical transport model over Canada and the USA. *Atmos. Chem. Phys.*, 14:4065–4077, 2014.
- [23] K. U. Goss. Comment on "Influence of soot carbon on the soil-air partitioning of polycyclic aromatic hydrocarbon". *Environmental Science & Technology*, 38(5):1622–1623, 2004.
- [24] K. U. Goss. The pka values of pfoa and other highly fluorinated carboxylic acids. *Environ. Sci. Technol.*, 42:456–458, 2008.
- [25] C. J. Halsall, A. J. Sweetman, L. A. Barrie, and K. C. Jones. Modelling the behaviour of PAHs during atmospheric transport from the UK to the Arctic. *Atmos. Environ.*, 35:255–267, 2001. 392TU ATMOS ENVIRON.
- [26] C.J. Halsall, L.A. Barrie, P. Fellin, D.G.C Muir, B.N. Billeck, L. Lockhart, F. Rovinsky, E. Kononov, and B. Pastukhov. Spatial and temporal variation of polycyclic aromatic hydrocarbons in the Arctic atmosphere. *Environ. Sci. Technol.*, 31:3593–3599, 1997.
- [27] M. Houde, J. W. Martin, R. J. Letcher, K. R. Solomon, and D. C. G. Muir. Biological monitoring of polyfluoroalkyl substances: a review. *Environ. Sci. Technol.*, 40:3463–3473, 2006.
- [28] H. Hung, P. Blanchard, C. J. Halsall, T. F. Bidleman, G. A. Stern, P. Fellin, D. C. G. Muir, L. A. Barrie, L. M. Jantunen, P. A. Helm, J. Ma, and A. Konoplev. Temporal and spatial variabilities of atmospheric polychlorinated biphenyls (PCBs), organochlorine (OC) pesticides and polycyclic aromatic hydrocarbons (PAHs) in the Canadian Arctic: Results from a decade of monitoring. *Science of the Total Environment*, 342(1-3):119–144, 2005. Sp. Iss. SI.
- [29] Haley Hung, Matthew MacLeod, Ramon Guardans, Martin Scheringer, Ricardo Barra, Tom Harner, and Gan Zhang. Toward the next generation of air quality monitoring: Persistent organic pollutants. *Atmos. Environ.*, 80:591–598, 2013.
- [30] S. S. Isukapalli, S. Balakrishnan, and P. G. Georgopoulos. Computationally efficient uncertainty propagation and reduction using the stochastic response surface method. *43rd IEEE Conference on Decision and Control*, 2:2237–2243, 2004.
- [31] T.F. Kahan, N.-O.A. Kwamena, and D.J. Donaldson. Heterogeneous ozonation kinetics of polycyclic aromatic hydrocarbons on organic films. *Atmos. Environ.*, 40:3448–3459, 2006.

- [32] S.M. Kazakov, M.N. Kaputerko, and V.A. Suchkov. Determination of first ionization potentials from spectra of electronic energy loss in the vapor of polyatomic organic compounds. *Journal of Applied Spectroscopy*, 66(3):375–379, 1999.
- [33] E. S. C. Kwok, W. P. Harger, J. Arey, and R. Atkinson. Reactions of Gas-Phase Phenanthrene under Simulated Atmospheric Conditions. *Environmental Science & Technology*, 28(3):521–527, 1994. MZ607 ENVIRON SCI TECHNOL.
- [34] G Lammel, A.M. Sehili, T.C. Bond, J Feichter, and H Grassl. Gas/particle partitioning and global distribution of polycyclic aromatic hydrocarbons- A modelling approach. *Chemosphere*, 76:98–106, 2009.
- [35] H Liu, D.J. Jacob, I Bey, and R.M. Yantosca. Constraints from 210pb and 7be on wet deposition and transport in a global three-dimensional chemical tracer model driven by assimilated meteorological fields. *J. Geophys. Res.*, 106(D11):12,109–12,128, 2001.
- [36] R. Lohmann and G. Lammel. Adsorptive and absorptive contributions to the gas-particle partitioning of polycyclic aromatic hydrocarbons: State of knowledge and recommended parametrization for modeling. *Environ. Sci. Technol.*, 38:3793–3803, 2004.
- [37] D. D. Lucas and R. G. Prinn. Parametric sensitivity and uncertainty analysis of dimethylsulfide oxidation in the clear-sky remote marine boundary layer. *Atmos. Chem. Phys.*, 5:1505–1525, 2005.
- [38] R. W. Macdonald, L. A. Barrie, T. F. Bidleman, M. L. Diamond, D. J. Gregor, R. G. Semkin, W. M. Strachan, Y. F. Li, F. Wania, M. Alaee, L. B. Alexeeva, S. M. Backus, R. Bailey, J. M. Bowers, C. Gobeil, C. J. Halsall, T. Harner, J. T. Hoff, L. M. Jantunen, W. L. Lockhart, D. Mackay, D. C. Muir, J. Pudykiewicz, K. J. Reimer, J. N. Smith, and G. A. Stern. Contaminants in the Canadian Arctic: 5 years of progress in understanding sources, occurrence and pathways. *Sci Total Environ*, 254(2-3):93–234, 2000.
- [39] J. W. Martin, S. A. Mabury, K. R. Solomon, and D. C. G. Muir. Bioconcentration and tissue distribution of perfluorinated acids in rainbow trout. *Environ. Toxicol. Chem.*, 22:196–204, 2003.
- [40] J. W. Martin, S. A. Mabury, K. R. Solomon, and D. C. G. Muir. Dietary accumulations of perfluorinated acids in juvenile rainbow trout. *Environ. Toxicol. Chem.*, 22:189–195, 2003.
- [41] Torsten Meyer and Frank Wania. What environmental fate processes have the strongest influence on a completely persistent organic chemical’s accumulation in the Arctic? *Atmos. Environ.*, 41:2757–2767, 2007.
- [42] NIST. Webbook benzo[a]pyrene (accessed jun 29,2014). <http://webbook.nist.gov/cgi/cbook.cgi?ID=C50328&Mask=20>.

- [43] B. D. Phenix, J. L. Dinero, M. A. Tatang, J. W. Tester, J. B. Howard, and G. J. McRae. Incorporation of parametric uncertainty into complex kinetic mechanisms: Application to hydrogen oxidation in supercritical water. *Combust. Flame*, 112:132–146, 1998.
- [44] Asif Qureshi, Matthew MacLeod, and Konrad Hungerbühler. Quantifying uncertainties in the global mass balance of mercury. *Global Biogeochem. Cycles*, 25:GB4012, 2011.
- [45] G. Russell. Monthly latitude insolation. data.giss.nasa.gov/ar5/srmonlat.html.
- [46] U. Schenker, M. Scheringer, and K. Hungerbühler. Including degradation products of persistent organic pollutants in a global multi-media box model. *Environ. Sci. Pollut. Res.*, 14:145–152, 2007.
- [47] U. Schenker, M. Scheringer, M.D. Sohn, R.L. Maddalena, T.E. McKone, and K. Hungerbühler. Using information on uncertainty to improve environmental fate modeling: A case study on DDT. *Environ. Sci. Technol.*, 43:128–134, 2009.
- [48] M. Scheringer, F. Wegmann, K. Fenner, and K. Hungerbühler. Investigation of the cold condensation of persistent organic pollutants with a global multimedia fate model. *Environ. Sci. Technol.*, 34:1842–1850, 2000.
- [49] B. F. Scott, C. Spencer, S. A. Mabury, and D. C. G. Muir. Poly- and perfluorinated carboxylates in north american precipitation. *Environ. Sci. Technol.*
- [50] A.M. Sehili and G Lammel. Global fate and distribution of polycyclic aromatic hydrocarbons emitted from Europe and Russia. *Atmos. Environ.*, 41:8301–8315, 2007.
- [51] J. H. Seinfeld and S. N. Pandis. *Atmospheric Chemistry and Physics: From Air Pollution to Climate Change*. Wiley, 2006.
- [52] D.T. Shindell, M. Chin, F. Dentener, R. M. Doherty, G. Faluvegi, A.M. Fiore, P. Hess, D. M. Koch, I.A. MacKenzie, M. G. Sanderson, M. G. Schultz, M. Schultz, D. S. Stevenson, H. Teich, C. Textor, O. Wild, D. J. Bergmann, I. Bey, H. Bian, C. Cuvelier, B. N. Duncan, G. Folberth, L. W. Horowitz, J. Jonson, J.W. Kaminski, E. Marmer, R. Park, K. J. Pringle, S. Schroeder, S. Szopa, T. Takemura, G. Zeng, T. J. Keating, and A. Zuber. A multi-model assessment of pollution transport to the Arctic. *Atmos. Chem. Phys.*, 8:5353–5372, 2008.
- [53] W.-Y. Shiu and K.-C. Ma. Temperature dependence of physical-chemical properties of selected chemicals of environmental interest. I. Mononuclear and polynuclear aromatic hydrocarbons. *J. Phys. Chem. Ref. Data*, 29:41–130, 2000.
- [54] M. Shoeib, T. Harner, and P. Vlahos. Perfluorinated chemicals in the arctic atmosphere. *Environ. Sci. Technol.*, 40:7577–7583, 2006.

- [55] I. Stemmler and G. Lammel. Pathways of pfoa to the arctic: variabilities and contributions of oceanic currents and atmospheric transport and chemistry sources. *Atmos. Chem. Phys.*, 10:9965–9980, 2010.
- [56] N. L. Stock, V. I. Furdui, D. C. G. Muir, and S. A. Mabury. Perfluoroalkyl contaminants in the canadian arctic: Evidence of atmospheric transport and local contamination. *Environ. Sci. Technol.*, 41:3529–3536, 2007.
- [57] M. A. Tatang, W. Pan, R. G. Prinn, and G. J. McRae. An efficient method for parametric uncertainty analysis of numerical geophysical models. *J. Geophys. Res.*, 102:21925–21932, 1997.
- [58] C. P. Thackray, C. L. Friedman, Y. Zhang, and N. E. Selin. Quantitative assessment of parametric uncertainty in northern hemisphere pah concentrations. *Environ. Sci. Technol.*, 49:9185–9193, 2015.
- [59] UNECE. Protocol to the 1979 Convention on Long-Range Transboundary Air Pollution on Persistent Organic Pollutants. Technical report, United Nations Economic Commission for Europe, 1998.
- [60] L. Vierke, C. Staude, A. Biegel-Engler, W. Drost, and C. Schulte. Perfluorooctanoic acid (pfoa) - main concerns and regulatory developments in europe from an environmental point of view. *Environmental Sciences Europe*, 24:1–11, 2012.
- [61] T. J. Wallington, M. D. Hurley, J. Xia, D. J. Wuebbles, S. Sillman, A. Ito, J. E. Penner, D. A. Ellis, J. Martin, S. A. Mabury, O. J. Nielsen, and M. P. S. Andersen. Formation of c7f15cooh (pfoa) and other perfluorocarboxylic acids during the atmospheric oxidation of 8:2 fluorotelomer alcohol. *Environ. Sci. Technol.*, 40:924–930, 2006.
- [62] Q Wang, D.J. Jacob, J.A. Fisher, J Mao, E.M. Leibensperger, C.C. Carouge, P Le Sager, Y Kondo, J.L. Jimenez, M.J. Cubison, and S.J. Doherty. Sources of carbonaceous aerosols and deposited black carbon in the Arctic in winter-spring: implications for radiative forcing. *Atmos. Chem. Phys.*, 11:12453–12473, 2011.
- [63] Y. Wang, D. J. Jacob, and J. A. Logan. Global simulation of tropospheric o3-ox-hydrocarbon chemistry, 1. model formulation. *J. Geophys. Res.*, 103:10713–10726, 1998.
- [64] Z. Wang, I. T. Cousins, M. Scheringer, R. C. Buck, and K. Hungerbuhler. Global emission inventories for c4-c14 perfluoroalkyl carboxylic acid (pfca) homologues from 1951 to 2030, part i: production and emissions from quantifiable sources. *Environment International*, 70:62–75, 2014.
- [65] Z. Wang, I. T. Cousins, M. Scheringer, R. C. Buck, and K. Hungerbuhler. Global emission inventories for c4-c14 perfluoroalkyl carboxylic acid (pfca) homologues from 1951 to 2030, part ii: The remaining pieces of the puzzle. *Environment International*, 69:166–176, 2014.

- [66] F. Wania. A global mass balance analysis of the source of perfluorocarboxylic acids in the arctic ocean. *Environ. Sci. Technol.*, 41:4529–4535, 2007.
- [67] F Wania and D Mackay. A global distribution model for persistent organic chemicals. *Sci. Total Environ.*, 161:211–232, 1995. QD143 SCI TOTAL ENVIR.
- [68] R. L. Waterland and K. D. Dobbs. Atmospheric chemistry of linear perfluorinated aldehydes: Dissociation kinetics of $\text{C}_n\text{F}_{2n+1}\text{CO}$ radicals. *J. Phys. Chem. A*, 111:2555–2562, 2007.
- [69] Henry Wohrnschimmel, Matthew MacLeod, and Konrad Hungerbuhler. Emissions, Fate and Transport of Persistent Organic Pollutants to the Arctic in a Changing Global Climate. *Environ Sci Technol.*, 47:2323–2330, 2013.
- [70] S. Wu, L.J. Mickley, D.J. Jacob, J.A. Logan, R.M. Yantosca, and D. Rind. Why are there large differences between models in global budgets of tropospheric ozone? *J. Geophys. Res.*, 112(D05302), 2007.
- [71] Z. Xie, Z. Wang, W. Mi, A. Moller, H. Wolschke, and R. Ebinghaus. Neutral poly-/perfluoroalkyl substances in air and snow from the arctic. *Scientific Reports*, 5, 2015.
- [72] G. Yarwood, S. Kemball-Cook, M. Keinath, R. L. Waterland, S. H. Korzeniowski, R. C. Buck, M. H. Russell, and S. T. Washburn. High-resolution atmospheric modeling of fluorotelomer alcohols and perfluorocarboxylic acids in the north american troposphere. *Environ. Sci. Technol.*, 41:5756–5762, 2007.
- [73] C. J. Young, V. I. Furdul, J. Franklin, R. M. Koerner, D. C. G. Muir, and S. A. Mabury. Perfluorinated acids in arctic snow: New evidence for atmospheric formation. *Environ. Sci. Technol.*, 41:3455–3461, 2007.
- [74] C. J. Young, M. D. Hurley, T. J. Wallington, and S. A. Mabury. Atmospheric chemistry of 4:2 fluorotelomer iodide ($\text{C}_4\text{F}_9\text{CH}_2\text{CH}_2\text{I}$): kinetics and products of photolysis and reaction with OH radicals and Cl atoms. *J. Phys. Chem. A*, 112:13542–13548, 2008.
- [75] C. J. Young and S. A. Mabury. Atmospheric perfluorinated acid precursors: Chemistry, occurrence, and impacts. *Reviews of environmental contamination and toxicology*, 208:1–109, 2010.
- [76] Y Zhang and S Tao. Global atmospheric emission inventory of polycyclic aromatic hydrocarbons (PAHs) for 2004. *Atmos. Environ.*, 43:812–819, 2009.